

1

2

3

4

Cosmic ray validation of electrode positions in small-strip thin gap chambers for the upgrade of the ATLAS detector

5

Lia Formenti

6

7

8

Department of Physics
McGill University, Montreal
October, 2021

9

10

11

12

13

A thesis submitted to
McGill University
in partial fulfillment of the
requirements of the degree of
Master of Science

¹⁵ Table of Contents

¹⁶	1	Introduction	1
¹⁷	2	High energy particle physics	4
¹⁸	2.1	The Standard Model	4
¹⁹	2.2	Beyond the Standard Model	6
²⁰	2.3	Studying high energy particle physics with accelerators	7
²¹	3	The LHC and the ATLAS experiment	9
²²	3.1	The Large Hadron Collider	9
²³	3.2	Luminosity	9
²⁴	3.3	The High-luminosity LHC	10
²⁵	3.4	The ATLAS experiment	12
²⁶	4	The New Small Wheels	17
²⁷	4.1	Motivation for the New Small Wheels (NSWs)	17
²⁸	4.2	Design of the NSWs	19
²⁹	4.3	Small-strip thin gap chambers	21
³⁰	4.4	sTGC Quadruplet Construction	22
³¹	4.5	NSW alignment	25

32	5 Using cosmic muons to measure relative strip position offsets	28
33	5.1 Cosmic rays	28
34	5.2 Experimental setup	29
35	5.3 Data acquisition	30
36	5.4 Data preparation	30
37	5.4.1 Cuts on electrode hits	30
38	5.4.2 Clustering and tracking	31
39	5.5 Measuring relative local offsets	33
40	5.6 Visualizing relative alignment between layers	36
41	5.7 Systematic uncertainty	38
42	5.8 Discussion	40
43	6 Using x-rays to measure relative strip position offsets	41
44	6.1 Experimental setup	41
45	6.2 Data acquisition	43
46	6.3 Data preparation	43
47	6.4 Measuring local offsets	43
48	6.5 Measuring relative local offsets	45
49	7 Comparing cosmic muon and x-ray relative strip position offsets	49
50	7.1 Assessing correlation	49
51	7.2 Discussion	54
52	8 Outlook and summary	56
53	8.1 Outlook	56
54	8.2 Summary	57
55	References	58
56	APPENDICES	66

57	A Cluster position uncertainty	67
58	A.1 Cluster definition	67
59	A.2 Effect of fit algorithm on cluster mean	67
60	A.3 Effect of uncertainty in cluster mean on track residuals	68
61	B Analysis statistics	69
62	C Analysis systematics	71
63	C.1 Residual distribution fit function	71
64	C.2 Cosmic muon data collection voltage	72
65	C.3 Cluster fit algorithm	74
66	C.4 Differential non-linearity	75
67	D Printable plots	78

Abstract

69 The Large Hadron Collider (LHC) is used to generate subatomic physics processes at the
70 energy frontier to challenge our understanding of the Standard Model of particle physics.
71 The particle collision rate at the LHC will be increased up to seven times its design value in
72 2025-2027 by an extensive upgrade program. The innermost endcaps of the ATLAS muon
73 spectrometer consist of two wheels of muon detectors that must be replaced to maintain
74 the muon momentum resolution in the high-rate environment. The so-called New Small
75 Wheels (NSWs) are made of two detector technologies: micromegas and small-strip thin gap
76 chambers (sTGCs). The sTGCs are gas ionization chambers that hold a thin volume of gas
77 between two cathode boards. One board is segmented into copper readout strips of 3.2 mm
78 pitch that are used to precisely reconstruct the coordinate of a passing muon. Modules of
79 four sTGCs glued together into quadruplets cover the NSWs. Quadruplets were designed
80 to achieve a 1 mrad angular resolution to fulfill the spectrometer's triggering and precision
81 tracking requirements. To achieve the required angular resolution the absolute position of
82 the readout strips must be known in the ATLAS coordinate system to within 100 μm . At
83 McGill University, the performance of sTGC quadruplets was characterized using cosmic ray
84 data before being sent to CERN, where the charge profile left by x-rays is used to measure
85 the offset of the strip patterns with respect to nominal at a limited number of points on
86 the surface of each quadruplet. The x-ray strip position measurements have acceptable but
87 limited precision and do not span the whole area of the strip layers. Given the importance of
88 knowing the absolute position of each readout strip to achieve the performance requirements
89 of the NSWs, the x-ray method must be validated by an independent method. Cosmic ray
90 data is used to characterize the relative alignment between layers and validate the x-ray
91 method.

Résumé

Le collisioneur LHC est utilisé pour générer des processus de la physique subatomique à la frontière d'énergie pour remettre en cause le modèle standard de la physique des particules. Le taux des collisions du collisioneur LHC augmentera jusqu'à sept fois le taux nominal en 2025-2027 par un programme d'amélioration majeur et varié. Une partie du spectromètre à muons est composée de deux roues de détecteurs de muons qu'il faut remplacer pour maintenir la résolution d'élan après l'augmentation du taux. Appelées les Nouvelles Petites Roues (NSWs), elles en utilisent deux technologies: des chambres micromegas et des chambres sTGCs (chambres à petites bandes et à intervalles fins). Les sTGCs sont des chambres d'ionisation de gaz, qui contiennent un volume de gaz fin entre deux panneaux cathodiques. Un panneau est segmenté à petites bandes en cuivre avec une pente de 3.2 mm qui se servent comme des voies de signal pour reconstruire précisément la coordonnée d'un muon qui passe. Des modules de quatre sTGCs collés ensemble en quadruplets couvrent les NSWs. Les quadruplets étaient conçus pour réaliser une résolution angulaire de 1 mrad pour satisfaire les exigences des systèmes de déclenchement et de mesures de précision. Pour réaliser la résolution angulaire il faut que la position absolue de chaque bande soit connue dans ATLAS avec une précision à moins de 100 μm . À l'Université de McGill, la performance des quadruplets étaient caractériser avec des rayons cosmiques avant les envoyer à CERN, où le profil de charge laisser par des rayons-X est utilisé pour mesurer le déplacement du motif des bandes par rapport à nominal à un nombre de position limité sur la surface des quadruplets. Les déplacements mesurés pas les rayons-X ont une précision acceptable mais limitée, et ne couvrent pas la région entière des panneaux. Étant donné l'importance de savoir la position absolue de chaque bande pour réaliser les exigences de performance des NSWs, il faut une méthode indépendante pour valider la méthode des rayons-X. Les données recueillies avec les rayons cosmiques sont utilisées pour charactariser l'alignement relatif entre les panneaux et pour valider la méthode des rayons-X.

Acknowledgements

- 119 Experimental particle physics projects are never done alone. I am grateful to have been
120 working with the ATLAS Collaboration for two years now.
- 121 Thank you to Dr. Brigitte Vachon for her guidance throughout this project and for editing
122 this thesis. I am consistently amazed by her ability to jump into the details of my project
123 and discuss them with me.
- 124 Thanks also to Dr. Benoit Lefebvre, who collected some of the data used in this thesis, wrote
125 several software tools I used to analyze the data and advised me several times throughout
126 this project.
- 127 Thank you to my labmates at McGill University, Dr. Tony Kwan, Kathrin Brunner, John
128 McGowan and Charlie Chen. Kathrin taught me mechanical skills that I will apply elsewhere.
129 Tony, manager of the laboratory, created the most encouraging, trusting and productive work
130 environment I have ever been apart of.
- 131 Thank you to the friends I can call on at anytime, and thank you to my family whose
132 constant support makes every step possible.

Contribution of authors

¹³⁴ I, the author, was involved in collecting the cosmic ray data from September 2019 - March
¹³⁵ 2021. I did not design the cosmic ray testing procedure nor write the data preparation
¹³⁶ software, but I participated in using the software to analyze cosmic ray results. In the
¹³⁷ thesis, the terms “clustering,” “local offset” and “relative local offset” are defined. Cosmic
¹³⁸ ray clustering was done in the data preparation software, but I redid the fit afterwards to
¹³⁹ explore sensitivity to the fit algorithm. With help from Dr. Lefebvre and Dr. Vachon, I
¹⁴⁰ helped design the software that calculated the relative local offsets from cosmic ray data.
¹⁴¹ I wrote that software on my own. I was not involved in the design, data collection, data
¹⁴² preparation or analysis of the x-ray data. I also was not involved in creating an alignment
¹⁴³ model from the x-ray data. I used the x-ray local offsets calculated using x-ray data analysis
¹⁴⁴ software to calculate relative local offsets with x-rays. I did the comparison between the
¹⁴⁵ x-ray and cosmic ray data.

¹⁴⁶ I hereby declare that I am the sole author of this thesis. This is a true copy of the thesis,
¹⁴⁷ including any required final revisions, as accepted by my examiners.

¹⁴⁸

Chapter 1

¹⁴⁹

Introduction

¹⁵⁰ The Standard Model (SM) is a theoretical framework that describes experimental observa-
¹⁵¹ tions of particles and their interactions at the smallest distance scales; however, the questions
¹⁵² the SM does not address motivate more experimentation.

¹⁵³ Accelerators collide particles to generate interactions that can be recorded by detectors
¹⁵⁴ for further study. Detectors measure the trajectory and energy of all secondary particles
¹⁵⁵ produced in collisions to understand the interaction. The Large Hadron Collider (LHC) [1]
¹⁵⁶ at CERN is the world’s most energetic particle accelerator. Its energy makes it a unique
¹⁵⁷ tool to study elementary particles and their interactions in an environment with conditions
¹⁵⁸ similar to what would have existed in the early universe. If study at the energy frontier is
¹⁵⁹ to continue, the LHC must go on.

¹⁶⁰ After 2025, the statistical gain in running the LHC further without significant increase in
¹⁶¹ beam intensity will become marginal. The High Luminosity Large Hadron Collider (HL-
¹⁶² LHC) project [2] is a series of upgrades to LHC infrastructure that will allow the LHC
¹⁶³ to collect approximately ten times more data than in the initial design by \sim 2030. The
¹⁶⁴ increase in LHC beam intensity will result in a large increase in collision rate that will make
¹⁶⁵ accessible and improve statistics on several measurements of interest [3], many only possible
¹⁶⁶ at the LHC and the energy frontier. The increase in beam intensity will also increase the
¹⁶⁷ level of background radiation, requiring major upgrades to the experiments used to record
¹⁶⁸ the outcomes of the particle collisions.

¹⁶⁹ The ATLAS experiment [4] is one of the LHC’s general-purpose particle detector arrays, po-
¹⁷⁰ sitioned around one of the collision points of the LHC. During the 2019-2022 Long Shutdown
¹⁷¹ of the LHC, the most complex upgrade of the ATLAS experiment is the replacement of the
¹⁷² small wheels of the muon spectrometer with the so-called New Small Wheels (NSWs) [5].

173 The detector upgrade addresses both the expected decrease in hit efficiency of the precision
174 tracking detectors and the high fake trigger rate expected in the muon spectrometer at the
175 HL-LHC. The NSWs are made of two different detector technologies: micromegas and small-
176 strip thin gap chambers (sTGCs). Micromegas are optimized for precision tracking while
177 sTGCs are optimized for rapid triggering, although each will provide complete coverage and
178 measurement redundancy over the area of the NSWs. Eight layers each of sTGCs cover the
179 NSWs. Practically, countries involved in detector constructor created quadruplet modules of
180 four sTGCs glued together that were arranged and installed over the area of the NSWs once
181 they arrived at CERN. Teams across three Canadian institutions built and characterized 1/4
182 of all the required sTGCs.

183 The sTGCs are gas ionization chambers that consist of a thin volume of gas held between two
184 cathode boards. One board is segmented into strip readout electrodes of 3.2 mm pitch. The
185 position of the particle track in the precision coordinate can be reconstructed from the strip
186 signals [5]. The sTGCs achieved the design track spatial resolution in the precision coordinate
187 of less than 100 μm per detector plane that will allow them to achieve a 1 mrad track angular
188 resolution using the 8 layers of sTGC on the NSW [6, 5]. The NSW measurement of the
189 muon track angle will be provided to the ATLAS trigger and used to reject tracks that do
190 not originate from the interaction point [5].

191 The precise measurement of a muon track angle depends on knowing the position of each
192 readout strip within the ATLAS coordinate system. To achieve this, the position of specific
193 locations on the surface of sTGC quadruplets will be monitored by the ATLAS alignment
194 system to account for time-dependent deformations [5]. Within a quadruplet module, the
195 strip positions could have been shifted off of nominal by non-conformities of the strip pattern
196 etched onto each cathode boards [7] and shifts between strip layers while gluing sTGCs into
197 quadruplets.

198 An x-ray gun was used to measure the offset of strips from their nominal position at the
199 locations that will be monitored by the ATLAS alignment system thereby providing, locally,
200 an absolute “as-built” strip position within the ATLAS coordinate system. Estimates of the
201 “as-built” positions of every readout strip are obtained by building an alignment model from
202 the available x-ray measurements [8].

203 The technique of measuring the “as-built” strip positions using x-ray data has never been
204 used before and must be validated. This thesis describes the use of cosmic muon data,
205 recorded to characterize the performance of each Canadian-made sTGC module, to validate
206 the x-ray strip position measurements. A description of how this work fits within the overall
207 alignment scheme of the NSW is also presented.

208 *Rewrite after implementing Brigitte’s edits.* Chapters 3 and 4 give more background on
209 particle physics, the LHC, ATLAS, the NSWs, and sTGCs. In chapter 5, the cosmic ray

210 testing procedure and how the position of the strips can be probed with cosmics data is
211 presented. Chapter 6 introduces the x-ray method, and in chapter 7, the x-ray offsets are
212 validated with cosmic muon data. The thesis concludes with a summary and outlook in
213 chapter 8.

²¹⁴ **Chapter 2**

²¹⁵ **High energy particle physics**

- ²¹⁶ Particle physics aims to study the elementary constituents of matter. Understanding the
²¹⁷ fundamental building blocks and how they interact provides insights into the evolution of
²¹⁸ the early universe to the forms of matter we observe today. This chapter introduces general
²¹⁹ concepts in particle physics relevant to understanding the physics goals of the HL-LHC and
²²⁰ NSW upgrade.
- ²²¹ The information on particle physics and the SM presented here is rather general; the reader
²²² is referred to [9, 10, 11] for more information.

²²³ **2.1 The Standard Model**

- ²²⁴ The Standard Model (SM) is the theoretical framework developed in the early 1970's to
²²⁵ describe the observed elementary particles and their interactions. It is built on a collection
²²⁶ of quantum field theories and has been remarkably successful at predicting experimental
²²⁷ observations, including but not limited to, the existence of the top quark [12], the tau
²²⁸ neutrino [13] and the Higgs boson [14, 15].
- ²²⁹ The known elementary particles described by the SM are represented in figure 2.1. There
²³⁰ are 12 matter particles (six quarks and six leptons), 4 force-mediating particles, and the
²³¹ Higgs boson. Each matter particle also has an anti-matter particle pair with the same
²³² mass but opposite charge, not represented in figure 2.1. The different forces of nature are
²³³ understood to be the result of the exchange of force-mediating particles between interacting
²³⁴ (coupled) particles. Photons are mediators of the electromagnetic force, W⁺/- and Z bosons
²³⁵ are mediators of the weak force, and gluons are mediators of the strong force. At high

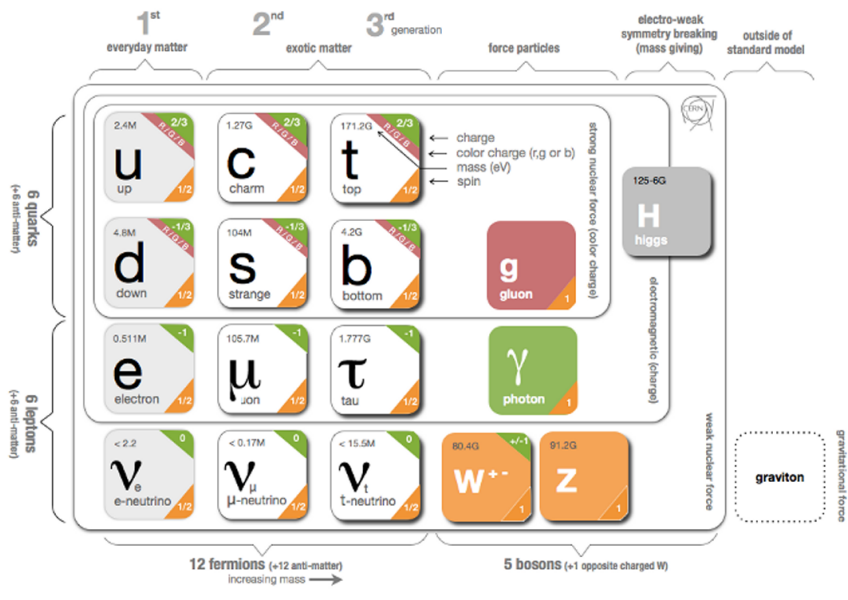


Figure 2.1: Schematic diagram of all elementary particles in the SM. Particles are grouped according to their properties and the forces through which they interact with other particles [16].

236 energy, the SM describes the electromagnetic and weak forces as stemming from a unified
237 electroweak force.. The Higgs boson field interacts with the particles mediating the unified
238 electroweak force to distinguish the weak and electromagnetic forces from each other at lower
239 energies and give particles (except neutrinos) a mass. This is called electroweak symmetry
240 breaking.

241 Quarks are matter particles that are sensitive to all forces; notably they are the only particles
242 sensitive to the strong force. Protons and neutrons are made up of quarks and gluons, and
243 the strong force is responsible for their existence and mutual attraction into nuclei [17].
244 Leptons are particles not sensitive to the strong force. Charged leptons include the electron,
245 which once part of atoms is responsible for chemistry. Of particular importance for this
246 thesis is the charged lepton called a muon. It is like the electron but its mass is \sim 200 times
247 larger than that of the electron. Muons have a lifetime of $2.2 \mu\text{s}$ [11] and decay predominantly
248 as $\mu \rightarrow e^-\bar{\nu}_e\nu_\mu$. Neutrinos are neutral, almost massless leptons that only interact through
249 the weak force.

250 Common matter is made up of the lightest constituents of the SM: up and down quarks,
251 electrons and photons. The other particles are produced in high-energy environments but
252 then decay to the lightest constituents. Such high energy environments include the condi-
253 tions present in the early universe [18], astrophysical sources, and particle accelerators. The
254 presence of the particles of the SM at the beginning of the Universe means that their inter-
255 actions and decays are fundamental for the study of the evolution of the early universe [18].
256 Many high energy astrophysical sources, like supernovae, generate particles that rain down
257 on Earth as cosmic rays [19]. Particle accelerators have been built to create controlled envi-
258 ronments of high-rate particle collisions at high energy where the production and decay of
259 elementary particles can be directly studied..

260 2.2 Beyond the Standard Model

261 Despite its success at describing most experimental observations to date, there is ample
262 evidence that the SM is not a complete description of natural phenomena at the smallest
263 scales. For example, the SM has a large number of free parameters, the values of which have
264 to be fine-tuned to fit experimental observations. This is part of the so-called “naturalness”
265 problem.

266 Furthermore, the SM provides no explanation for several open questions in particle physics.
267 First, neutrinos in the SM are assumed to be massless and do not gain mass in the same way
268 as the other particles. However, in 2013 neutrino were confirmed to change between their
269 different flavours [20], which can only occur if neutrinos do have mass [21]. The neutrino

270 mass requires physics beyond the standard model [22]. Second, several astrophysical and
271 cosmological measurements suggest the presence of “dark matter” making up 85 % of the
272 matter content of the universe [23]. The nature of dark matter is unknown and so far there is
273 no SM explanation [24]. Third, the SM does not explain the origin and nature of the matter-
274 antimatter asymmetry that produced our matter-dominated universe. Finally, the SM does
275 not include a description of gravity.

276 Theoretical extensions beyond the Standard Model (BSM) aim to address some of these
277 questions, often predicting existence of yet-unseen elementary particles and/or physics phe-
278 nomena beyond those predicted by the SM. For example, super-symmetry (SUSY) predicts
279 that each SM particle has a heavier super-symmetric partner. SUSY would explain the
280 origin of dark matter with weakly interacting massive particles, would solve the so-called
281 “naturalness” problem in the SM [25]. These hypothetical new physics phenomena and/or
282 new particles can be searched for at particle accelerators.

283 **2.3 Studying high energy particle physics with accel- 284 erators**

285 In particular, particle accelerators of increasingly higher energy have a long history of en-
286 abling the discovery of predicted, yet-unseen particles. These include, for example, the
287 discovery of the W [26, 27] and Z bosons [28, 29], the top quark [30, 31], and most recently,
288 the discovery of the Higgs boson [32, 33] marking the completion of the SM as it is known
289 today.

290 Based on the established success of the SM, there are two approaches to particle physics
291 research. One approach is to search for the existence of new physics phenomena predicted
292 to exist in BSM theories and the other is to test the validity of the SM to a high degree of
293 accuracy to search for flaws in the model. Standard Model predictions are generally expressed
294 in terms of the probability of a specific physics process to occur, expressed as a cross section
295 in units of barns (with 1 barn = 10^{-28} m²). As an example, figure 2.1 shows a summary
296 of cross section measured for different physics processes using the ATLAS experiment and
297 their comparison with the predictions of the SM. Most cross section measurements agree
298 well within one standard deviation with the SM predictions.

299 Particle accelerators provide a controlled and high-collision rate environment that makes
300 them ideal places to search for new physics phenomena and to carry out systematic tests of
301 the SM. The LHC is the highest energy collider in the world so it can access physics that no
302 other accelerator can, notably the direct production of the Higgs boson and top quark. A
303 description of the LHC and the ATLAS detector are provided in the next chapter.

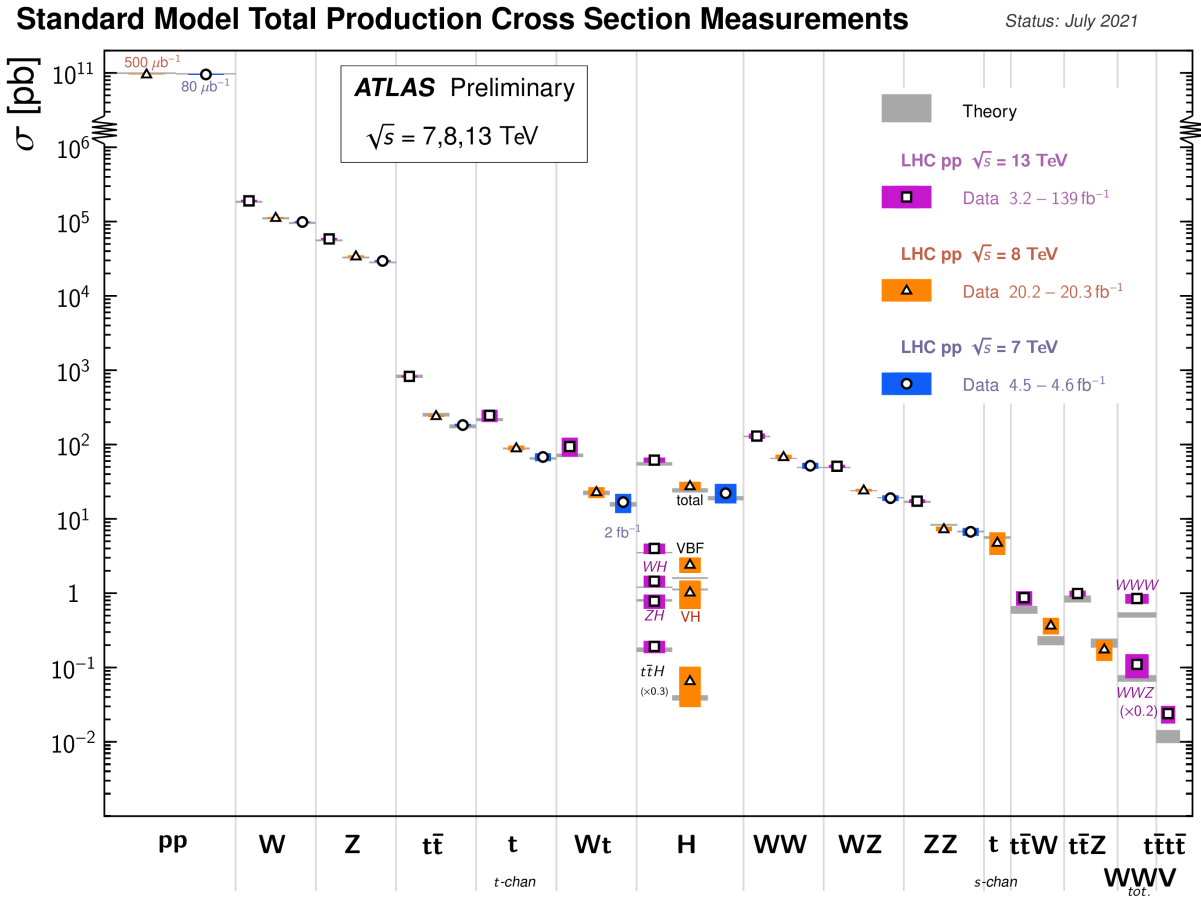


Figure 2.2: Production cross sections of different final states measured by the ATLAS experiment at the LHC. Comparison with the SM theory predictions is also shown [34].

304 **Chapter 3**

305 **The LHC and the ATLAS experiment**

306 **AN INTRODUCTION**

307 **3.1 The Large Hadron Collider**

308 The LHC is an accelerator 27 km in circumference and located \sim 100 m underground at
309 CERN near Geneva, Switzerland [1]. It has two beam pipes that counter-circulate bunches
310 of protons¹ before colliding the bunches in the center of one of four major experiments, such
311 as the ATLAS experiment (discussed in section 3.4). In the previous run of the LHC (run-2),
312 protons were collided with a center of mass energy of 13 TeV. It is not actually the protons
313 that interact, but the constituent quarks and gluons (partons) that each carry some fraction
314 of the energy and momentum of the collisions.

315 **3.2 Luminosity**

316 The number of proton-proton interactions generated by the LHC directly affects the statistics
317 available to make measurements of cross sections, SM parameters, etc. Predicting the
318 number of proton-proton interactions requires defining a metric called luminosity [11]. It is

¹the LHC also accelerates lead ions, but ATLAS is best at recording proton-proton collisions. The ALICE experiment [35] was designed for lead-lead interactions.

319 the number of particles an accelerator can send through a given area per unit time. It is
320 calculated from the measurable quantities in equation 3.1:

$$\mathcal{L} = \frac{f N_1 N_2}{4\pi\sigma_x\sigma_y} \quad (3.1)$$

321 f is the frequency of the bunch crossings (25 ns), N_1 and N_2 are the number of protons in
322 each bunch ($\sim 10^{11}$ protons / bunch), and σ_x and σ_y are the RMS of the spatial distributions
323 of the bunch. Therefore, luminosity is a property of accelerator beams, which are set by the
324 capabilities of the accelerator. The design luminosity of the LHC was $10^{34} \text{ cm}^{-2}\text{s}^{-1}$. The
325 units of luminosity are an inverse area; multiplying the luminosity by the cross section of a
326 given process gives the expected rate for that process.

327 Integrating the *instantaneous* luminosity (equation 3.1) over a period of data collection gives
328 the integrated luminosity,

$$L = \int \mathcal{L}(t) dt \quad (3.2)$$

329 which is related to the total number of interactions. In this way, the luminosity is the link
330 between the accelerator and the statistical power of measurements to be made with the data
331 collected. So far, the LHC provided an integrated luminosity of 28.26 fb^{-1} in run-1 [36] and
332 156 fb^{-1} in run-2 [37].

333 3.3 The High-luminosity LHC

334 The HL-LHC upgrade [2] was accepted because without increasing the luminosity of the LHC
335 tenfold, running the accelerator will not provide significant statistical gain on measurements.
336 Also, some systems will need repair and replacement to operate past ~ 2020 . The LHC will
337 be the most energetic accelerator in the world for years to come and is the only accelerator
338 capable of directly producing the Higgs boson (and top quarks), so the European Strategy for
339 Particle Physics made it a priority “to fully exploit the physics potential of the LHC” with
340 “a major luminosity upgrade” [38]. The goal is for the HL-LHC to provide an integrated
341 luminosity of 3000 fb^{-1} in the 12 years following the upgrade. The luminosity actually
342 achieved will depend on a combination of technological advances and upgrades in progress
343 that affect the factors contributing to luminosity defined in equation 3.1 [2].

344 The most anticipated measurement at the HL-LHC is of the triple-Higgs coupling. Measuring
345 the coupling allows the shape of the Higgs potential responsible for electroweak symmetry



Figure 3.1: LHC/HL-LHC plan [39]. The integrated luminosities collected and projected for each run of the LHC are shown in blue boxes below the timeline and the center of mass energy of the collisions is shown in red above the timeline. The top blue arrow labels the run number. “LS” stands for “long shutdown” and indicates periods where the accelerator is not operating. During the shutdowns, upgrades to the LHC and the experiments are being installed. This timeline was last updated in January, 2021, and reflects changes in the schedule due to the ongoing pandemic.

346 breaking to be measured. Any discrepancy with the SM prediction will show that there
347 must be other sources of electroweak symmetry breaking, and hence currently unpredicted
348 particles. The LHC is the only accelerator where the Higgs can be produced directly and
349 the HL-LHC upgrade is required to have sufficient di-Higgs production to make a meaningful
350 measurement [3, 40]. Accordingly, detector sensitivity to various Higgs decays will be
351 important at the HL-LHC.

352 3.4 The ATLAS experiment

353 The ATLAS experiment [4] was designed to support all the physics goals of the LHC. It is
354 44 m long and 25 m in diameter, and weighs 7000 tones. It is an array of particle detector
355 subsystems arranged concentrically around the beam pipe and centered around one of the
356 LHC’s interaction points (a place where the beams collide), as shown in figure 3.2. ATLAS is
357 cylindrical because it aims to provide 4π coverage around the interaction point. It is helpful
358 to separate the subsystems of ATLAS into the so-called “barrel” and “endcap”/“forward”
359 regions, referring to the cylindrical geometry.

360 For analysis, ATLAS is typically described in spherical coordinates. The azimuthal angle
361 ϕ is measured around the beampipe and the polar angle θ is measured from the beam
362 pipe. A more useful coordinate than θ is the pseudo-rapidity, $\eta = -\ln \tan(\theta/2)$, because
363 it approaches the rapidity of a particle when its momentum is much greater than its mass
364 and differences in rapidity are approximately invariant to a Lorentz boost parallel to the
365 beam. The range of η is 0 (perpendicular to the beam) to $\pm\infty$ (parallel to the beam, or the
366 z-direction). Typically, η is the physically interesting coordinate because the ϕ coordinate
367 follows the cylindrical symmetry of the beam.

368 ATLAS provides identification and kinematic measurements for each particle created after
369 the initial collision. Predictions made using SM and BSM theories can then be compared
370 to the data. Each subsystem of ATLAS collects certain information and a complete
371 description of each recorded collision can be assembled offline. An overview of the main
372 ATLAS subsystems is given below.

373 The inner detector

374 The inner detector [41, 42] (figure 3.3) is for precision tracking, vertex measurements and
375 electron identification. A 2 T solenoid with field parallel to the beam bends the track of
376 outgoing particles. The innermost part is made of high-resolution semiconductor pixel and
377 strip detectors while the outermost part are straw-tubes that generate and detect transition
378 radiation

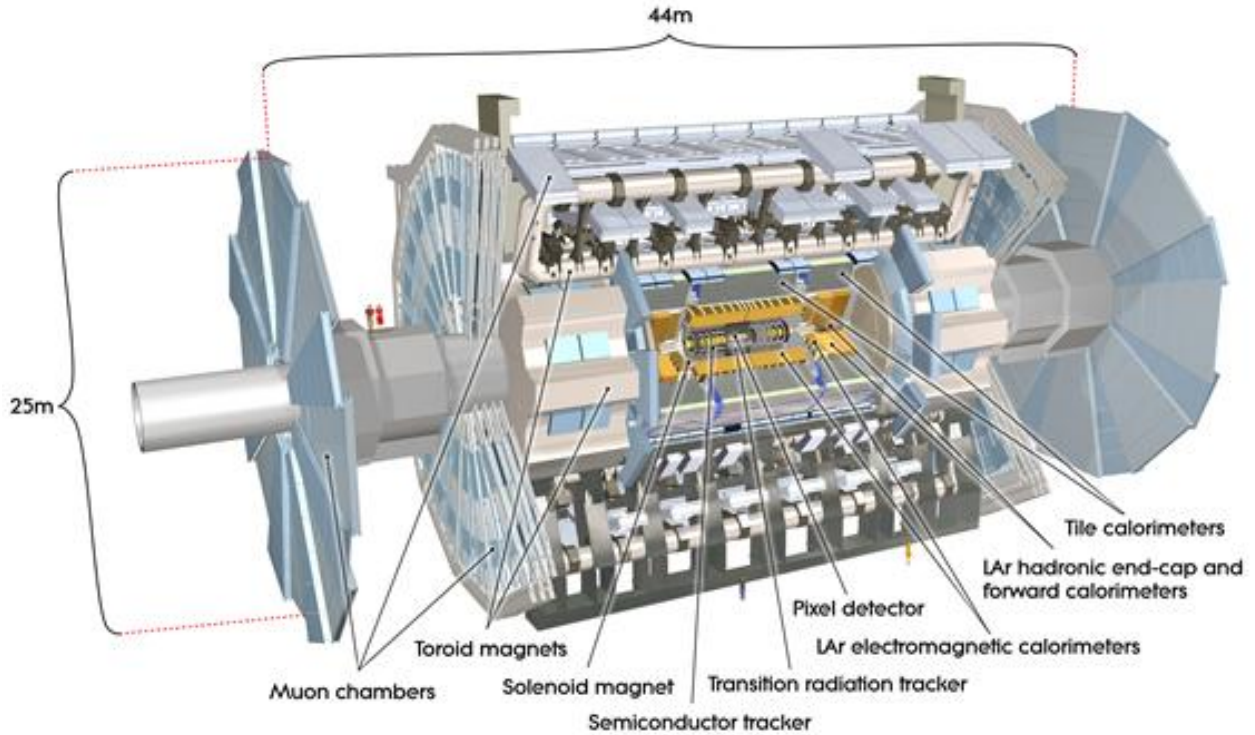


Figure 3.2: Diagram of the ATLAS experiment, with the various detector subsystems labelled [4].

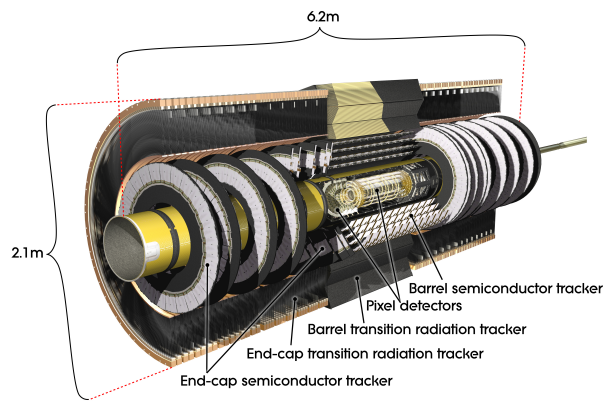


Figure 3.3: Diagram of the ATLAS experiment's inner detector, with the different segments and the technology used labelled [4].

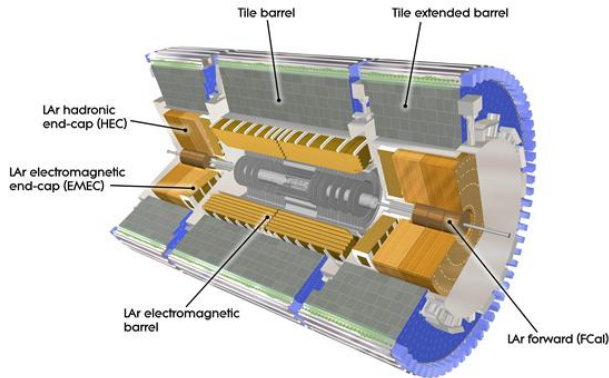


Figure 3.4: Diagram of the ATLAS calorimeter system, with the different segments and the technology used labelled [4].

379 Calorimetry system

380 Electromagnetic and hadronic sampling calorimeter units are used to record the energy
 381 of electrons, photons and jets. A combination of liquid-argon (LAr) electromagnetic and
 382 hadronic calorimeters [43] and tile-scintillator hadronic calorimeters [44] cover the rapidity
 383 range $|\eta| < 4.9$, as shown in figure 3.4.

384 The calorimeters cause incoming charged particles to shower and deposit their energy in
 385 the sensitive volume. Only muons and neutrinos are known to pass the calorimeters to the
 386 muon spectrometer. Particles other than those mentioned would have decayed in the inner
 387 detector before reaching the calorimeter.

388 Trigger system

389 It would be impossible to record all the data from bunch crossings every 25 ns, corresponding
 390 to a rate of ~ 40 MHz. ATLAS has a multi-level trigger system to select events of interest
 391 for permanent storage. The Level-1 (L1) hardware trigger [45] uses partial-granularity infor-
 392 mation from the muon spectrometer and calorimeter to trigger on high p_T muons, electrons,
 393 jets, high missing transverse energy, and τ decaying to hadrons. The maximum L1 trigger
 394 rate ATLAS can accommodate is 100 kHz with a latency of 2.5 μ s. After run-3 an upgrade
 395 of the trigger system will allow for a higher rate and more latency, but for now these are the
 396 working limits [46].

397 The L1 trigger is used to define regions of interest that are fed into the software high level
 398 trigger (HLT), in which the full granularity of the muon spectrometer and calorimeter are
 399 used with information from the inner detector to reduce the trigger rate to 1 kHz. Events

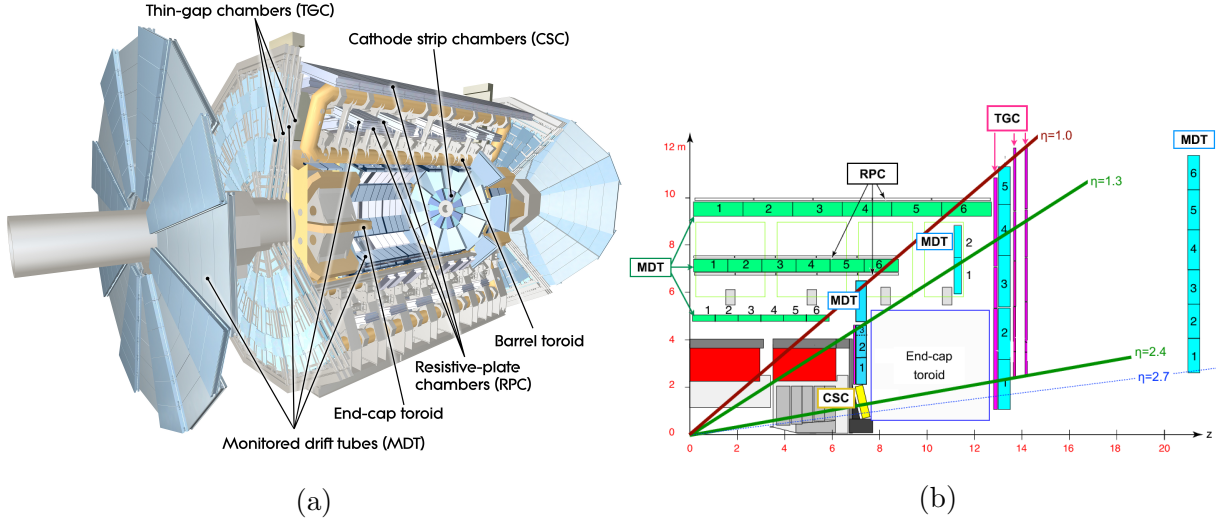


Figure 3.5: (a) The ATLAS muon spectrometer [4]. (b) A quarter-cut of ATLAS, with the interaction point in the bottom left corner. The small wheel is just left of the end cap toroid, the big wheel is to its right, and the outer wheel is the rightmost structure [50].

400 that pass the L1 and HLT trigger are recorded for use in offline analysis [47].
 401 The ATLAS trigger system is described in the references above but the trigger rates quoted
 402 here are after the upgrades implemented for run-2, described in [48].

403 Muon spectrometer

404 The muon spectrometer has multiple layers, each of which records the position of a pass-
 405 ing muon. Magnetic deflection by superconducting air-core toroid magnets bend the muon
 406 tracks. The position information recorded in each layer and the magnetic field are used to
 407 reconstruct each muon's momentum. In the barrel of ATLAS, eight coils bent into “race-
 408 tracks” arranged around the beampipe provide the magentic field. In the forward region,
 409 two end-cap toroids each with eight smaller racetrack-shaped coils arranged symmetrically
 410 around the beampipe are inserted in the ends of the barrel toroid [49]. Figure 3.5 shows the
 411 toroid magnets and the different parts of the ATLAS muon spectrometer [4].

412 The muon spectrometer [51] is separated into detectors used for precision offline tracking
 413 and for triggering. Three layers of monitored drift tubes (MDTs) or cathode strip chambers
 414 (CSCs) are used for tracking. The position of the muon track in each of the three layers allows
 415 reconstruction of the track and hence momentum. For the design momentum resolution of
 416 $\Delta p_T/p_T < 1 \times 10^{-4} p / \text{GeV}$ for $p_T < 300 \text{ GeV}$ and a few percent for lower p_T muons,

417 the MDTs and CSCs required position resolution of $50\text{ }\mu\text{m}$ each. Accordingly, an optical
418 alignment system was designed to monitor and correct for chamber positions [51, 52].

419 Resistive plate chambers (RPCs) are used for triggering in the barrel and thin-gap chambers
420 (TGCs) are used for triggering in the endcaps. The positions of each type of chamber are
421 sketched in figure 3.5b. Often, the endcap muon spectrometer is separated into three wheels –
422 the small wheel, big wheel, and outer wheel – ordered by proximity to the interaction point.
423 In run-1, low (high) p_T muons were triggered on at L1 if two (three) of the RPCs or TGCs
424 layers around the big wheel fired in coincidence, for the barrel and endcaps respectively [45].
425 After run-1 it was discovered that up to 90% of the triggers in the endcap were fake, caused
426 by background particles generated in the material between the small wheel and the big
427 wheel [5]. To reduce the fake rate in run-2, the TGCs on the inside of the small wheel also
428 had to register a hit. The added condition reduced the trigger rate by 50% in the range $1.3 < |\eta| < 1.9$ [48]. The effectiveness of the solution was limited since the $|\eta|$ -range of the small
429 wheel TGCs was limited to $1.0 < |\eta| < 1.9$ and the position resolution of the small wheel
430 TGCs is coarse [5].

432 **Chapter 4**

433 **The New Small Wheels**

434 **4.1 Motivation for the New Small Wheels (NSWs)**

435 The hit rate of all detector systems will increase with the HL-LHC not only because of the in-
436 crease in luminosity, but also because the background radiation rate increases proportionally
437 with luminosity. The combined rate presents problems for both the tracking and triggering
438 capabilities of the muon spectrometer [5].

439 In term of tracking, the efficiency of the MDTs decreases by 35% (mostly due to long dead-
440 times) already when exposed to the maximum hit rate at the current luminosity, 300 kHz.
441 At the threefold increase in luminosity predicted for run-3, most of the small wheel will be
442 subjected to a hit rate well above 300 kHz and it will begin missing hits. Losing hits in the
443 small wheel will reduce the high p_T muon momentum resolution. The decrease in resolution
444 will affect the ability to search for, for example, the decay of heavy bosons (W' , Z') or a
445 pseudo-scalar Higgs predicted by some SUSY models [3].

446 Already, the forward muon trigger system copes with a very high fake rate, even when
447 including TGC data from the small wheel in the trigger as in run-2. At the luminosity
448 expected in run-3, 60 kHz of the maximum 100 kHz of the L1 trigger would be taken by the
449 endcap muon spectrometer. A possible solution would be to raise the minimum p_T threshold
450 from 20 GeV to 40 GeV, but the ability to study several physics processes of interest depend
451 on low p_T muons, particularly the Higgs decay to two muons, the Higgs decay to two tau's
452 and SUSY particle decays to leptons [5].

453 The NSWs will solve both these problems. It will be covered with precision tracking cham-
454 bers suitable for the expected hit rates and triggering chambers capable of 1 mrad angular



Figure 4.1: A schematic of a quarter cross section of the ATLAS detector, with the collision/interaction point (IP) in the bottom left corner. Three possible tracks are labelled. Ideally, track A would be triggered on while track B and C discarded. With the small wheel, all three tracks would be recorded. With the NSW, only track A would be recorded [5].

resolution. The idea behind the triggering chambers is to match the small wheel track segment with the track segment from the big wheel to discard tracks not originating from the interaction point. Figure 4.1 illustrates this point: the run-1 trigger system would have triggered on all three tracks, while with the NSW the trigger system would only trigger on track A. Reducing the fake trigger rate means the NSWs will not miss as many muon hits and that the low p_T threshold will not have to be raised to cut particles not produced in the collision. The NSWs allow ATLAS to maintain the high p_T muon resolution and the low muon p_T threshold at the HL-LHC collision rate [5].

463 **4.2 Design of the NSWs**

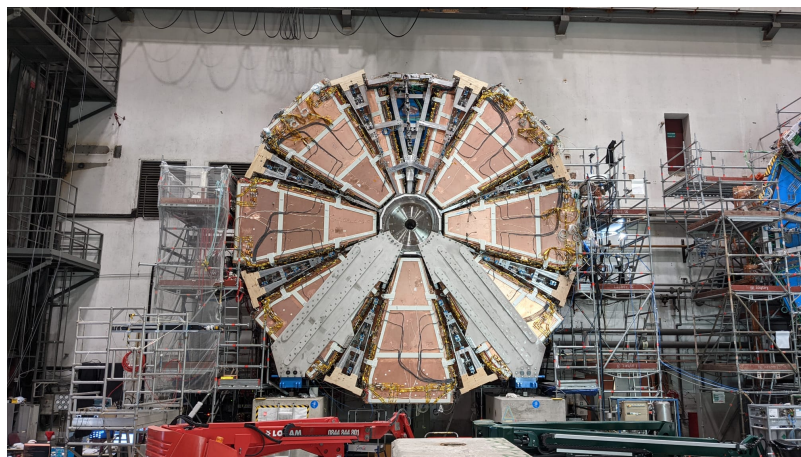
464 The NSWs are covered with two detector technologies: micromegas and small-strip thin gap
465 chambers. MMs are the primary tracking detectors and sTGCs are the primary triggering
466 detectors, but for redundancy sake both are designed to do either. Both sets of detectors are
467 to have position resolution better than $\sim 100 \mu\text{m}$ per plane. Four chambers of each type are
468 glued together to create quadruplet modules. Quadruplets of different sizes are assembled
469 into wedges. Two sTGC wedges and two MM wedges are layered to create sectors (with
470 the sTGC wedges on the outside) [5]. Different stages of the construction process are shown
471 in figure 4.2. At the time of writing, both NSWs have been assembled. The first has been
472 lowered into the ATLAS cavern and is being commissioned. The second will be lowered
473 shortly.



(a) An sTGC quadruplet module. The left image highlights the trapezoidal shape. The right image shows the short edge corner. The four sTGC layers and each layer's gas inlet are visible. The gas outlets and high voltage cables are at the long edge in the back of the photo. The green printed circuit board along the sides are the adaptor boards where the front end electronics are attached.



(b) Left: An sTGC wedge. The white frame outlines the individual quadruplet modules. Right: A completed sector, with two sTGC wedges on the outside and two MM wedges on the inside.



(c) The New Small Wheel. All sectors except one large sector at the top are installed, revealing two of the smaller sectors that are normally hidden under the large sectors and support bars. The NSWs are 10 m in diameter.

Figure 4.2: Images breaking down some of the construction units of the NSWs.



Figure 4.3: Internal structure of an sTGC, zoomed into the area under a pad. High voltage is applied to wires suspended in the gas volume to create an electric field. A passing muon causes an ionization avalanche that is picked up by the wire, strip and pad electrodes [8].

⁴⁷⁴ 4.3 Small-strip thin gap chambers

⁴⁷⁵ sTGCs are gas ionization chambers operated with a CO₂:n-pentane ratio of 55:45. Gold-
⁴⁷⁶ plated tungsten wires, 50 µm in diameter and with 1.8 mm pitch, are suspended between
⁴⁷⁷ two cathode planes made of FR-4, each 1.4 mm away (see figure 4.3). One cathode board is
⁴⁷⁸ segmented into pads of varying area (around 300 cm² each), and the other segmented into
⁴⁷⁹ strips of 3.2 mm pitch, perpendicular to the wires. High voltage is applied to the wires and
⁴⁸⁰ the cathode planes are grounded [5, 53]. When a muon passes through, the gas is ionized
⁴⁸¹ and the electric field in the gas gap causes an ionization avalanche [54]. The motion of the
⁴⁸² ions and electrons are picked up on the nearby wire, strip and pad electrodes [5]. The gas
⁴⁸³ mixture was chosen to absorb excess photons produced in the avalanche that delocalize the
⁴⁸⁴ avalanche signal [55]. The resistivity of the carbon coating and capacitance of the pre-preg

sheet tune the spread of the charge distribution [56] and the speed of the response [57] to optimize the rate capability. The hatching of the strips and wires establishes a coordinate system from which to extract the coordinate of the muon as it passes through the chamber. The small pitch of the strips is what allows the quadruplets to deliver good angular resolution to improve the fake trigger rate and meet the precision tracking requirements [5].

A 3-out-of-4 coincidence in pad electrodes from each layer of a quadruplet define a region of interest where the strip and wire electrodes should be readout. The pad triggering scheme greatly reduces the number of electrodes that require read-out so that a track segment of the required angular resolution can be provided quickly enough to the hardware trigger [5].

Signal is readout from groups of successive wires, so the position resolution in the direction perpendicular to the wires is 10 mm. The wires give the symmetric azimuthal coordinate in ATLAS so the position resolution in this direction is sufficient. Good resolution on the η coordinate, perpendicular to the strips, is important [5]. The average single chamber position resolution in the strip coordinate was 45 μm for perpendicular muon tracks as measured in a test beam [6] – well within design specifications. When four sTGCs are glued together into a quadruplet the design angular resolution of 1 mrad in the strip coordinate is achievable [5, 53].

Therefore, sTGCs are able to meet the triggering and precision tracking goals they were designed for. To ensure they can deliver once installed in ATLAS, knowing the position of the strips to within their position resolution in the ATLAS coordinate system is necessary. The NSW alignment system, detailed in section 4.5, monitors the position of alignment platforms installed on the surface of the wedges. The alignment platforms are installed with respect to an external reference on the sTGCs: two brass inserts on each strip layer on one of the angled sides of each quadruplet (shown in figure 4.4). So the challenge of positioning the strips in ATLAS was separated into two steps: first, position the strips with respect to the brass inserts; second use the alignment system to position the alignment platforms. The next section provides some pertinent details on the sTGC construction process, with steps that affect the position of the strips with respect to the brass inserts highlighted.

4.4 sTGC Quadruplet Construction

Five countries were responsible for producing the sTGC modules of varying geometries for the NSW: Canada, Chile, China, Israel and Russia. Canada was responsible for 1/4 of the required sTGCs, of three different quadruplet geometries. The steps of the construction process in each country were similar [5]. The process followed in Canada is detailed.

TRIUMF in Vancouver, British Columbia was responsible for preparing the cathode boards. The boards were made and the electrodes etched on at a commercial laboratory, Triangle



(a) Brass insert near long edge.

(b) Brass insert near short edge.

Figure 4.4: The brass inserts sticking out from the gas volumes of an sTGC quadruplet. These inserts were pressed against alignment pins when the individual sTGCs were being glued together.

519 Labs, in Carson City, Nevada. Once completed they were sent to TRIUMF to be sprayed with
520 graphite and otherwise prepared [7]. The boards are commercial multilayer printed circuit
521 boards, but the strip boards required precision machining to etch the strip pattern [5].
522 Triangle Labs also machined the two brass inserts into each strip board. A coordinate
523 measuring machine (CMM) was used to digitize a set of reference strips. Four quality
524 parameters describing non-conformities in the strip pattern of each board with respect to
525 the brass inserts were derived from the data and the results are available on a QA/QC
526 database. The parameters and the CMM data collection is described in full in [7]. Due to
527 time constraints, tolerances on the non-conformities in the etched strip pattern with respect
528 to the brass inserts were loosened, with the condition that the strip positions in ATLAS
529 would have to be corrected for [7].

530 The prepared boards were sent to Carleton University in Ottawa, Ontario for construction
531 into sTGCs and quadruplets. First, the wires were wound around the pad cathode boards
532 using a rotating table and the wires were soldered into place. A wound pad cathode board
533 was held by vacuum on a granite table, flat to within 20 μm , and a strip cathode board glued
534 on top to create an sTGC. Holding one sTGC flat with the vacuum, another was glued on
535 top to create a doublet, then two doublets were glued together to create a quadruplet. When
536 gluing sTGCs together, the brass inserts were pushed against alignment pins with the goal of
537 keeping the strip layers aligned within tolerance. However, non-conformities in the shape of
538 the brass inserts, non-conformities in the position of the alignment pins and shifts between
539 sTGCs while the glue cured resulted in misalignments between the brass inserts and strip
540 layers. Precise alignment of the pad boards or wires with respect to the strip boards did not
541 have to be so tightly controlled because pads do not measure the precision coordinate.

542 The Carleton team finished the quadruplets by installing adaptor boards on the angled sides
543 of each layer that allow front end electronics to be attached. Completed quadruplets were
544 sent to McGill University where they were characterized with cosmic rays. The details of
545 cosmic ray testing are described in chapter 5. Tested quadruplets were sent to CERN where
546 they were assembled into wedges and alignment platforms installed. The alignment platforms
547 were installed using a jig positioned with respect to the brass inserts. Completed wedges
548 were assembled into sectors then installed on the NSWs.

549 The quadruplet construction process had two steps where strip positions could be shifted off
550 of nominal. At board-level, there could be non-conformities in the etched strip pattern with
551 respect to the brass inserts, described by the four quality parameters [7]. At the quadruplet
552 level, misalignments between the brass inserts and strips on different layers were introduced
553 during the gluing. The result was that the brass inserts were not a reliable reference point
554 and that the strips can be offset from their design position by up to hundreds of micrometers.
555 Offsets in strip positions from nominal in Canadian quadruplets were shown to be random [7],

so no one correction would suffice. The offsets must be measured and corrected for in the ATLAS offline software that does the precision tracking. Understanding the work ongoing to make measurements of offsets and correct for them requires understanding the strategy of the NSW alignment system.

4.5 NSW alignment

The idea of the NSW alignment system is presented in [5], but the details have only been presented internally so far. After the wedges are constructed, alignment platforms are installed on every sTGC quadruplet and optical fibres routed to them, as shown in figure 4.5. Light from the optical fibres will be monitored in real time by cameras (BCAMs) mounted on the alignment bars of the NSWs. The system will thus record the positions of the alignment platforms in the ATLAS coordinate system, accessible at any point during operation.

The original alignment scheme was to use the brass inserts as a reference between the alignment platforms and the individual strips, as shown in the solid arrows in figure 4.6 – this will no longer work. The position of the alignment platforms will be known thanks to the alignment system, so a different method to get the position of the strips with respect to the alignment platforms is currently in its final stages. It uses the yet-unmentioned x-ray dataset to calculate offsets of the strip pattern of an sTGC layer in a local area (local offset) with respect to the nominal geometry by analyzing the beam profile left by an x-ray gun attached to different positions on the alignment platforms. Effectively, the reference to the brass inserts is skipped, represented as the dashed line in figure 4.6. The alignment platforms provide the link to the nominal geometry because their position with respect to the strips can be calculated from the nominal geometric parameters assuming that the strips are perfectly etched and aligned. Cosmic muon track positions cannot be compared to the nominal geometry because the alignment platforms are not installed when cosmics data is collected, so there is no external reference to provide a link to the nominal geometry.

The x-ray method does not have the sensitivity to measure the offset of each strip from nominal, but instead the offset of the strip pattern in a local area around the position of the gun can be measured. *Local offsets* are used to build an alignment model for each strip layer. Formally defined, an alignment model is a set of parameters used to estimate the true position of a strip given its nominal position. The alignment model currently being worked on takes x-ray and CMM data as input to calculate an offset and rotation of each strip layer with respect to nominal [8]. The alignment parameters could be described as “global”, meaning over the whole layer instead of local. Without the x-ray dataset, there would be no input to the alignment model that takes into account inter-layer misalignments introduced

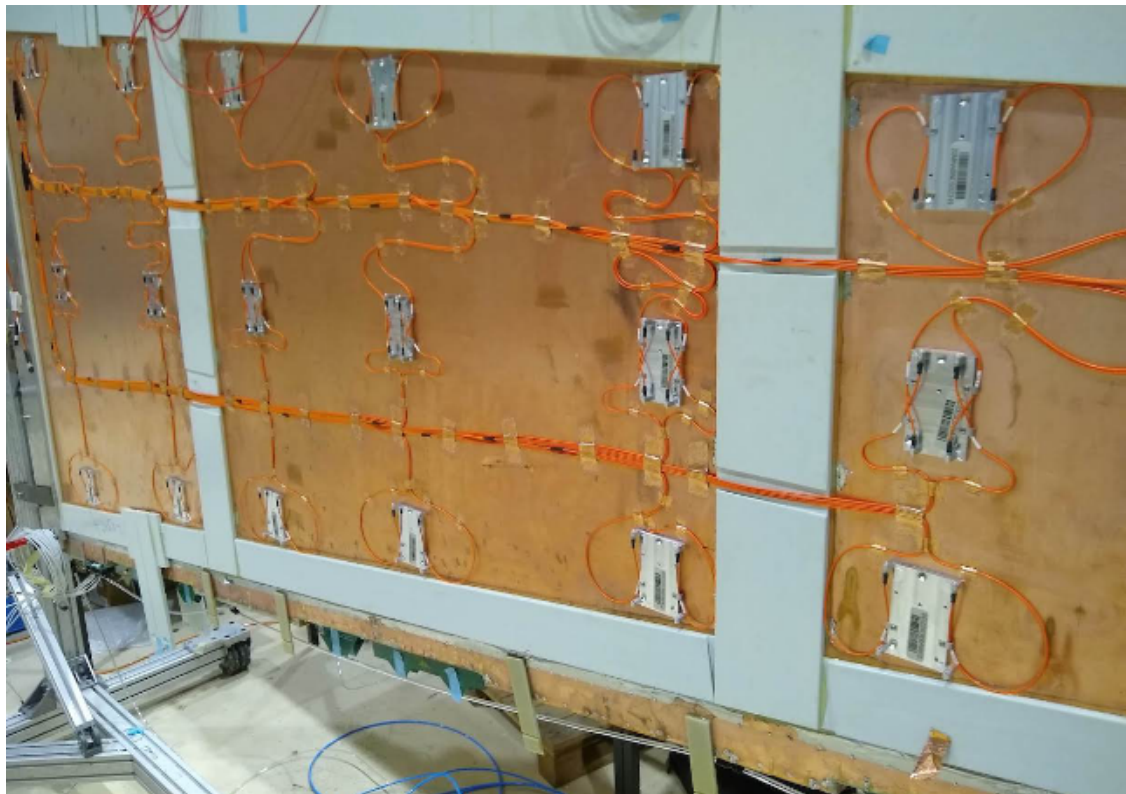


Figure 4.5: An sTGC wedge with alignment platforms (silver) installed on the quadruplet. Optical fibres (orange) are routed to the alignment platforms. Cameras on the frames of the NSWs will record light from the optical fibres to position the alignment platforms in the ATLAS coordinate system.

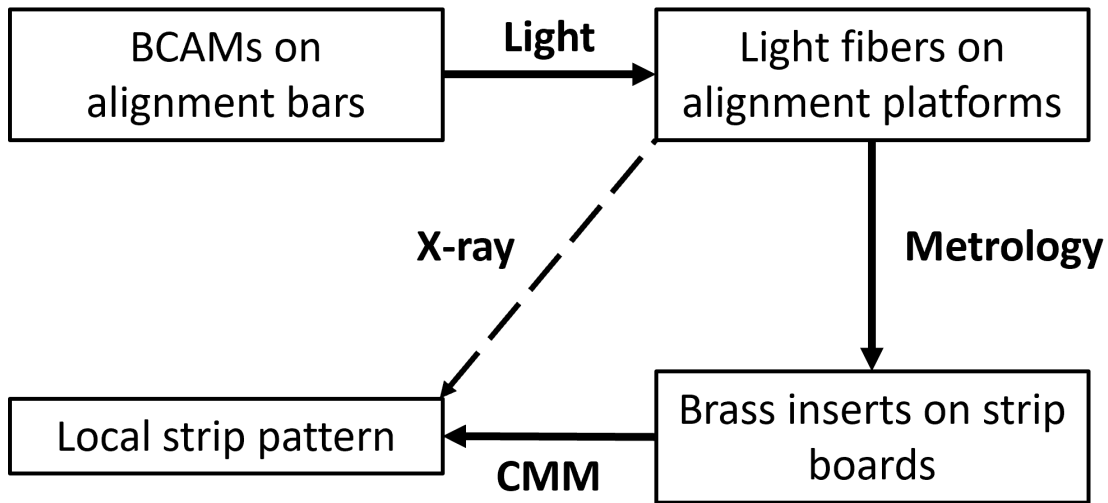


Figure 4.6: How the different elements of the sTGC alignment system relate to one another. The solid arrows denote the planned alignment scheme. The dashed arrow shows the modification being finalized now. This figure was originally designed by Dr. Benoit Lefebvre.

⁵⁹⁰ in construction.

⁵⁹¹ Given that the x-ray local offsets can only be measured at positions where the gun can be
⁵⁹² attached and that they are an important part of the alignment scheme, the x-ray method
⁵⁹³ needs to be validated. The goal of this thesis is to validate the x-ray local offsets while
⁵⁹⁴ exploring how cosmics data complements and adds to the understanding of strip positions
⁵⁹⁵ and overall alignment.

⁵⁹⁶ Chapter 5

⁵⁹⁷ Using cosmic muons to measure ⁵⁹⁸ relative strip position offsets

⁵⁹⁹ At McGill, among other quality and functionality tests, each Canadian-made quadruplet was
⁶⁰⁰ characterized with cosmic muons. In this chapter, the experimental setup and how the data
⁶⁰¹ was analyzed to provide relative strip position offsets is presented. The analysis method
⁶⁰² was motivated by the how it could be compared to data collected with the x-ray method
⁶⁰³ (chapter 6) but also stands alone as a characterization of the alignment between strips of
⁶⁰⁴ different layers. First, a brief introduction to cosmic rays.

⁶⁰⁵ 5.1 Cosmic rays

⁶⁰⁶ The Earth is being bombarded by particles from the sun, galactic sources and extra galactic
⁶⁰⁷ sources – collectively called cosmic rays [19, 11]. Cosmic rays are mostly protons, but also
⁶⁰⁸ heavier ions, gamma rays and the term sometimes includes neutrinos. The primary (initial)
⁶⁰⁹ cosmic ray interacts with the atmosphere causes electromagnetic and hadronic showers of
⁶¹⁰ particles. Hadronic showers result from the primary cosmic ray interacting strongly with the
⁶¹¹ target of the atmosphere and the most abundant products are pions. Charge pions mostly
⁶¹² decay to muons (there is a lesser contribution to the muon flux from kaons as well) [58].
⁶¹³ Thanks to time dilation extending the muon’s lifetime as measured on Earth, a flux of
⁶¹⁴ approximately 1 muon/cm²/ min reaches the ground [11]. Measuring the muon flux and
⁶¹⁵ energy spectrum reveals information about primary cosmic rays [58] which is interesting to
⁶¹⁶ high energy physicists and astrophysicists. The muon flux is also terribly convenient for
⁶¹⁷ testing muon detectors.

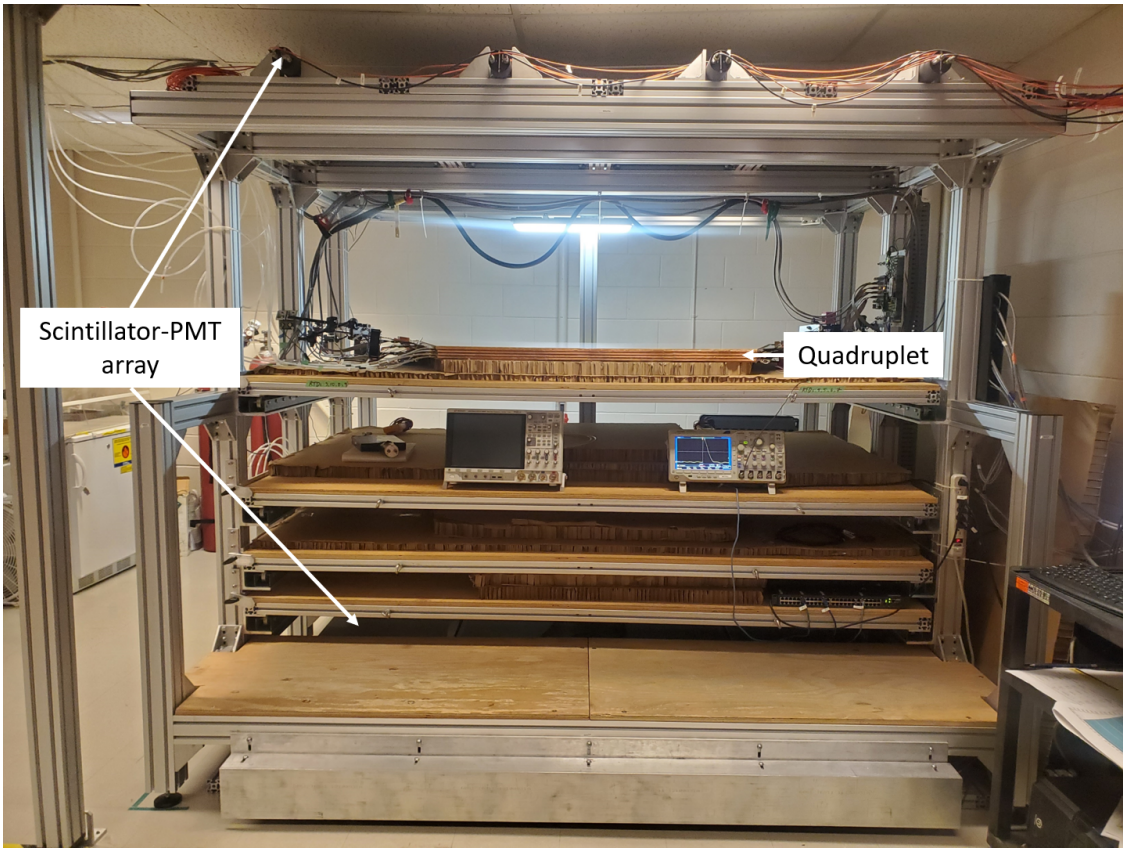


Figure 5.1: Cosmic muon hodoscope at McGill University with sTGC quadruplet in the test bench.

618 5.2 Experimental setup

619 Cosmic muon characterization was done with a hodoscope, a complete description of which
 620 can be found in [59]. The quadruplet was placed in the center of the test bench. Above
 621 and below it was a layer of scintillator-PMT arrays, labeled in figure 5.1. When a cosmic
 622 muon passed within the acceptance of the hodoscope, at least one scintillator from the top
 623 array and at least one from the bottom array fired in coincidence. The coincident signal was
 624 used to trigger the readout of the quadruplet's electrodes using NIM modules. The trigger
 625 was passed to the front-end electronics attached to the adaptor boards of each layer of the
 626 quadruplet.

627 Operating the chambers also required gas and high voltage. A pentane-CO₂ mixture was
 628 mixed and delivered to each sTGC with a gas system designed and made at McGill University.

629 The gas system was controlled by a slow control program, also made in-laboratory [60].
630 Although gas mixture is flammable, it allows the chambers to operate in high amplification
631 mode without production of excess photons saturating the signal across many strips because
632 pentane absorbs a wide energy of photons [55]. To prepare the quadruplets for operation,
633 CO_2 was flushed through them overnight to remove impurities. Then, five gas volumes of
634 the pentane- CO_2 mixture was flushed through (approximately 3 hours). High voltage was
635 provided by CAEN boards.

636 5.3 Data acquisition

637 Each sTGC electrode was connected to a channel on a prototype ASIC¹ on the front-end
638 electronics, attached to the adaptor boards on each layer of a quadruplet. The ASIC ampli-
639 fied the signal and was set to measure and record the signal peak amplitude from electrodes.
640 For each trigger, the signal peak amplitude of all channels above threshold was recorded
641 as an event and stored in a binary file. Channel thresholds were estimated [62] and ad-
642 justed manually in the configuration/readout software before the start of data acquisition.
643 There was an exception to the threshold rule: the signals on strips adjacent to a strip above
644 threshold were also readout using the so-called “neighbour triggering” function of the ASIC.
645 The quadruplets were held at 3.1 kV for approximately two hours to collect data from 1
646 million muon triggers.

647 5.4 Data preparation

648 5.4.1 Cuts on electrode hits

649 Corrupted data is removed while the raw data is being recorded in a binary file. The binary
650 file is decoded into a usable ROOT [63] tree offline.

651 A hit is defined as a signal recorded from a channel that was above threshold or (in the
652 case of strips) neighbour triggered. In addition to hits from muons, the quadruplets record
653 noise from the electronics and δ -rays (electrons liberated with sufficient energy to cause more
654 ionization before acceleration). Therefore, cuts are applied to reduce the number of noise
655 hits. The edge strips are very noisy, so all strip hits on layers with strip hits on either
656 edge channel are cut. A default pedestal value is subtracted from the recorded signal peak

¹the VMM3 [61], designed for the MMs and sTGCs of the NSW

amplitude of each electrode for a more realistic estimate of the signal amplitude. Also, events that only have hits on pad electrodes (no strips or wires) were cut because the large area of the pads made them susceptible to noise.

5.4.2 Clustering and tracking

Many of the high-level characterization metrics require rebuilding muon tracks. For events passing quality cuts, the x - and y -coordinates of the ionization avalanche on each layer are extracted from the signal on the wires and strips respectively for each event, as is sketched in figure 5.2. In this work, x is the coordinate perpendicular to the wires and y is the coordinate perpendicular to the strips.

The x -coordinate is taken as the center of the wire group with the maximum peak signal amplitude, since the wire groups' pitch (36 mm) is larger than the typical charge spreading. Assuming that the true x -position of the hit is sampled from a uniform distribution over the width of the wire group, the uncertainty in the x -position was given by $\frac{36}{\sqrt{12}}$ mm = 10 mm [64].

The y -coordinate is taken as the Gaussian mean of the peak signal amplitude distribution across groups of contiguous strips. The process of grouping contiguous strip hits on a layer is called clustering, and the resulting group is called a cluster. Figure 5.2 sketches the clustering process and a sample cluster is shown in figure 5.3. The data acquisition system recorded the electrode ID of the strip hit and in the clustering process the position of the center of the strip electrode is calculated based on the nominal quadruplet geometry. Typically, clusters are built of 3-5 strips. The thickness of the graphite coating over the cathode boards determined how many strips picked up the ionization image charge. Larger clusters were more likely caused by δ -rays since they spread the cloud of ionization.

Events are cut from the analysis if there are two clusters on one layer's set of strips (indicative of noise). Clusters are cut if the cluster size is lesser than three (which should not happen for real events thanks to neighbour triggering), and if the cluster size is greater than 25. After all the cuts on hits and clusters, roughly half as many muon tracks as triggers collected remain.

The uncertainty in the y -coordinate could have been taken as the fitted cluster mean's statistical uncertainty; however, after comparing the difference in cluster means for different fitting algorithms in appendix A.2, 60 μm of uncertainty was assigned.

The coordinates of the avalanches' on all layers were used to reconstruct tracks in x and y respectively. The tracks were then used to calculate characterization metrics like electrode efficiency and spatial resolution, the details of which are discussed in [59].

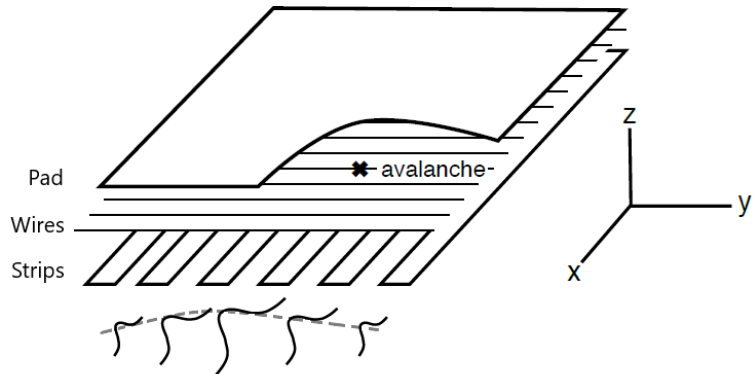


Figure 5.2: A sketch of an sTGC-like detector. The position of the avalanche is extracted from the wires and strips that picked up the avalanche signal. The signals on individual strips are sketched. Clustering was the processs of fitting a Gaussian to the peak value of the signals on individual contiguous strips, as is done in figure 5.3. In this work, the $x(y)$ -coordinate will always refer to the coordinate perpendicular to the wires (strips) [59, 56].

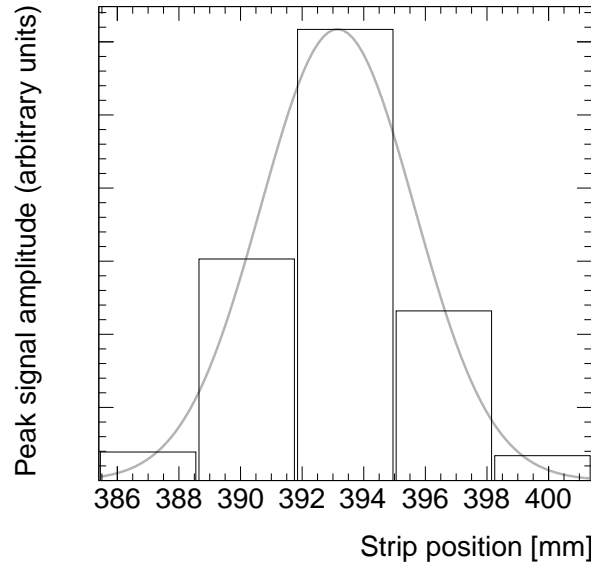


Figure 5.3: A sample cluster resulting from the current picked up on a group of strips after the passing of a muon (presumably). The grey curve is a Gaussian fit.

690 5.5 Measuring relative local offsets

691 The offset of a strip from its nominal position can be modeled as a passive transformation.
692 For each area of a strip layer, the local offset is the shift of the strip pattern in that area with
693 respect to the nominal geometry. Local offsets systematically change the set of strips nearest
694 to muons passing through the area. The data preparation software assumes that strips are
695 in their nominal positions, so the recorded muon y -position on layer i , y_i , is shifted opposite
696 to the layer's local offset, $d_{local,i}$, by

$$y_i = y_{nom,i} - d_{local,i}, \quad (5.1)$$

697 where $y_{nom,i}$ is the position of the muon that would have been recorded on layer i if there
698 was no local offset. Equation 5.1 ignores other factors that affect the cluster position, like
699 position resolution. With cosmics data, the local offset is unknown and there was no external
700 reference to measure $y_{nom,i}$. Therefore, only relative local offsets could be calculated.

701 The minimal relative coordinate system uses two reference or fixed layers [59]. The hits
702 on the two fixed layers were used to create tracks that can be interpolated or extrapolated
703 (polated) to the other two layers. The set of two fixed layers and the layer polated to are
704 referred to as a tracking combination. The residual of track i , Δ_i is defined as,

$$\Delta_i = y_i - y_{track,i}, \quad (5.2)$$

705 where $y_{track,i}$ is the polated track position. Track residuals are affected by the relative local
706 offset in the area of each layer's hit. As an example, in figure 5.4, the residual on layer
707 2 perhaps indicates that layer 2 is offset with respect to layers 1 and 4 in the area of the
708 track. Of course, a single track residual says nothing of the real relative local offset because
709 of the limited spatial resolution of the detectors and fake tracks caused by noise or delta
710 rays. However, the mean of residuals for all tracks in a region will be shifted systematically
711 by the local offsets between layers [59]. For a quadruplet with nominal geometry, the mean
712 of residuals should be zero in all regions and for all reference frames, unlike the example
713 regions in figure 5.5. The value of the mean of residuals is a measure of the relative local
714 offset of the layer with respect to the two fixed layers.

715 To study the relative local offsets, residual distributions across each strip layer of a quadruplet
716 for all tracking combinations were assembled and fitted. The residual distributions were
717 wider for tracking combinations where the extrapolation lever arm was largest, as in the
718 example distributions shown in figure 5.5. In general, residual means from distributions of
719 residuals with geometrically less favourable tracking combinations have larger statistical and
720 systematic uncertainties. The bin size of 200 μm for the distributions shown in figure 5.5 was

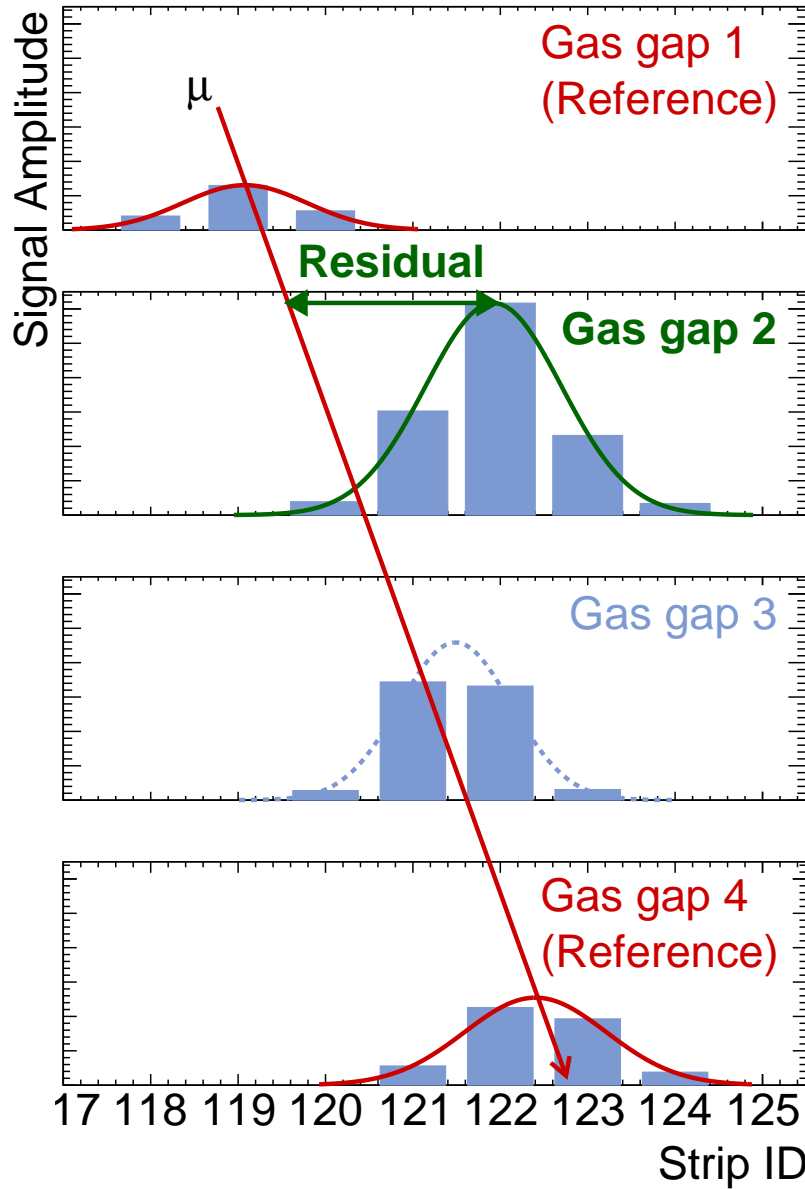
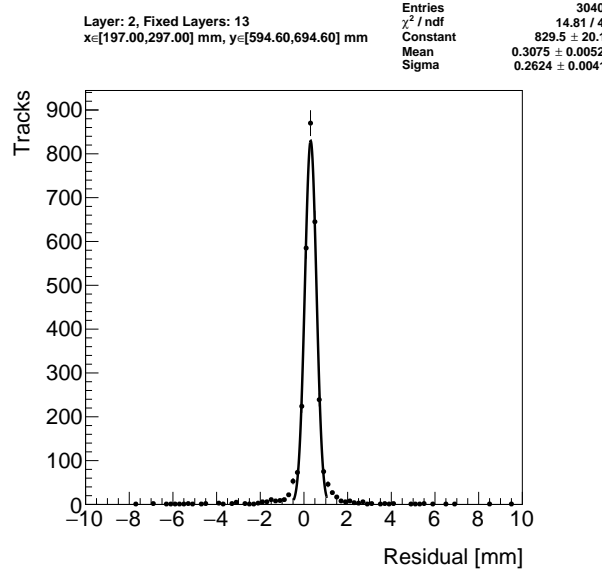
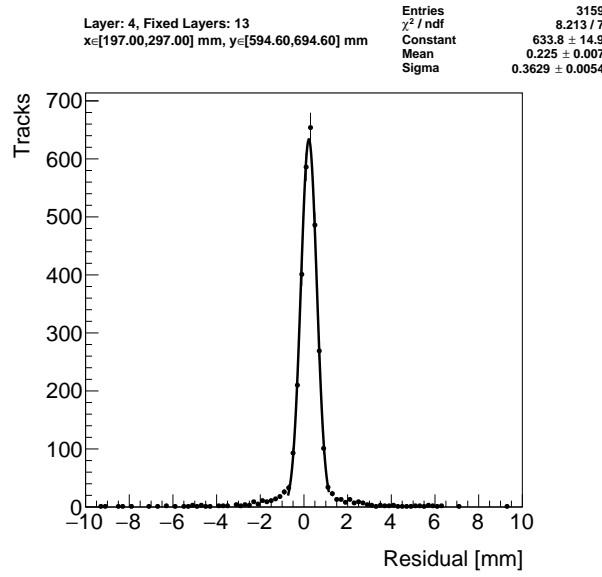


Figure 5.4: Representation of a muon event recorded by an sTGC. The clusters are fit with a Gaussian and the mean is taken as the hit position. A track is built from the chosen reference layers, 1 and 4, and the residual calculated on layer 2. The clusters come from a real muon, but their positions were modified to highlight the residual on layer 2.



(a) Tracks on layer 2, reference layers 1 and 3.



(b) Tracks on layer 4, reference layers 1 and 3.

Figure 5.5: Residual distribution in the region $x \in [197, 297]$, $y \in [594.6, 694.6]$ mm (100 mm by 100 mm area) for two different tracking combinations. Data from quadruplet QL2.P.11.

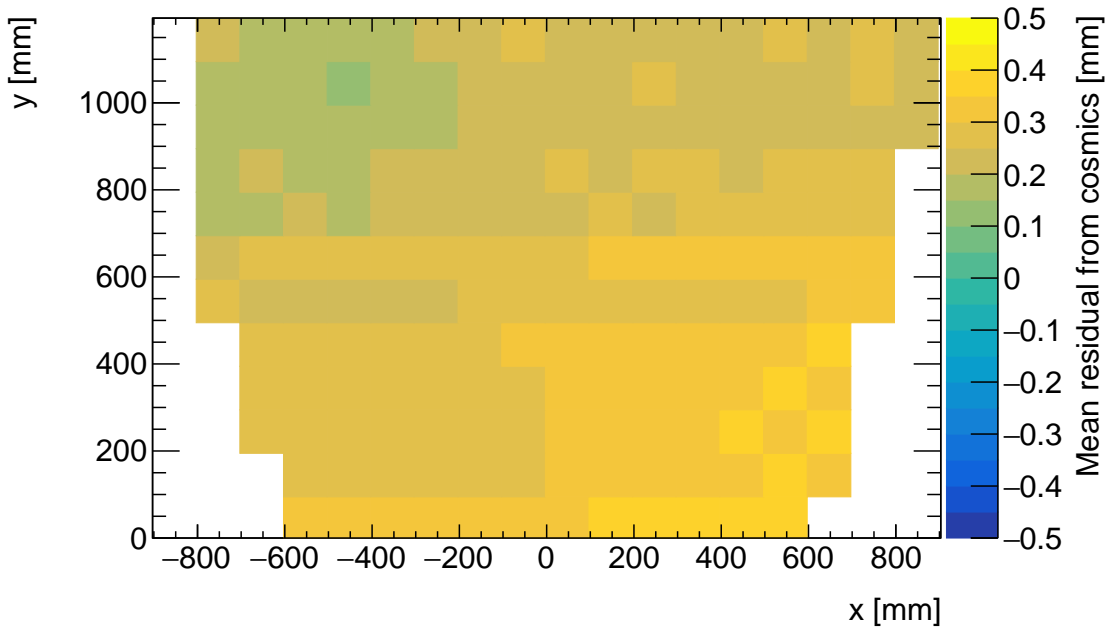
721 chosen based on the uncertainty on residuals calculated from tracks on layer 4 (1) built from
722 hits on layers 1 and 2 (3 and 4) given a cluster y -position uncertainty of $60\text{ }\mu\text{m}$ (appendix A.3),
723 since these tracks yield residuals with the largest uncertainties.

724 A gaussian fit was used to extract the mean of the residual distributions. Theoretically, a
725 double gaussian distribution is more apt, but for this analysis the gaussian fit was sufficient,
726 as discussed in appendix C.1.

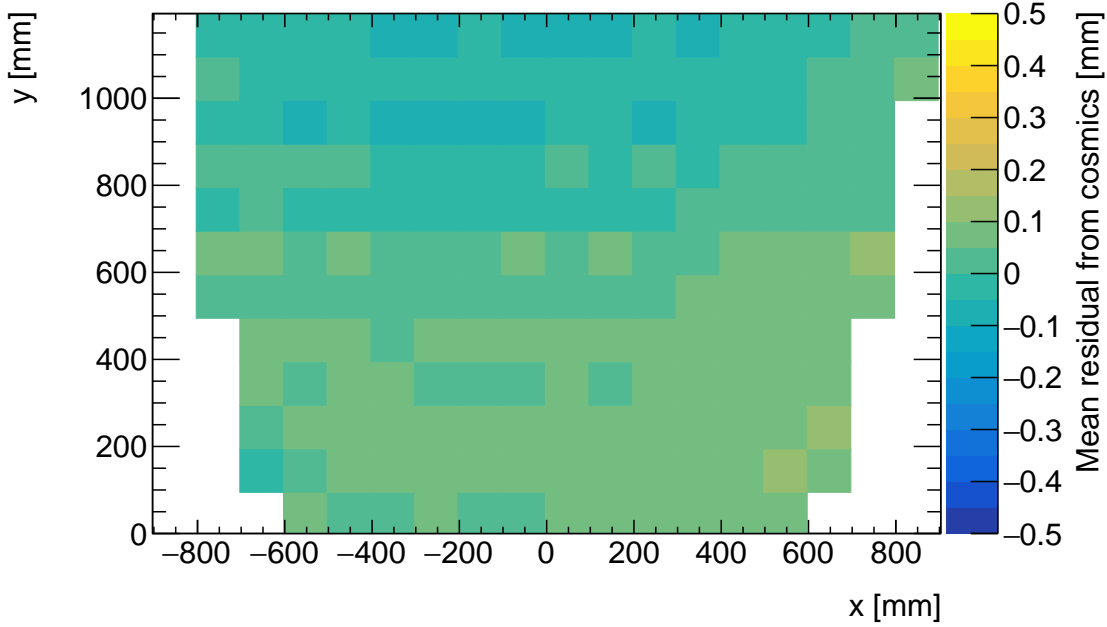
727 The area of the region of interest was 100 mm by 100 mm. The size balanced the amount of
728 tracks falling in the region of interest to give a small statistical uncertainty on the extracted
729 mean while being smaller than the order on which local offsets were expected to change
730 significantly. The change in local offsets over the surface of a layer can be modeled using
731 global alignment parameters. Using a base alignment model with a global offset and rotation
732 of each strip layer, “significantly” was defined by the distance in x that a large but possible
733 rotation of $1000\text{ }\mu\text{rad}$ would change the local offset by more than $50\text{ }\mu\text{m}$ – half the required
734 position resolution of the sTGCs [5].

735 5.6 Visualizing relative alignment between layers

736 The mean of residuals was plotted across entire strip layers for every tracking combination to
737 get a picture of the how relative local offsets change over the layers’ surface. Figure 5.6 shows
738 the mean of residuals on layer 2 with reference layers 1 and 3 for two different quadruplets,
739 referred to as QL2.P.11 and QL2.P.8, for 100 mm by 100 mm areas across the surface of
740 layer 2. To understand these plots, realize that the Gaussian mean of the distribution in
741 figure 5.5a is the entry in area bin $x \in [197, 297]$, $y \in [594.6, 694.6]$ mm in figure 5.6a.



(a) Mean of residuals of tracks on layer 2, reference layers 1 and 3, for QL2.P.11.



(b) Mean of residuals of tracks on layer 2, reference layers 1 and 3, for QL2.P.8.

Figure 5.6: Mean of residuals in each 100 mm by 100 mm bin over the area of the layer 2 cathode board. The entry in $x \in [197, 297]$, $y \in [594.6, 694.6]$ mm of figure 5.6a corresponds to the fitted Gaussian means in figures 5.5a. The mean of residuals is an estimate of the local offset of layer 2 with respect to layers 1 and 3.

742 Many of the residual means are non-zero and change smoothly over the layer, indicating
743 that there are relative local offsets stemming from misalignments between entire strip layers.
744 Given that the residual mean changes with x in figure 5.6a, there is likely a rotation of layer
745 2 with respect to layers 1 and 3 on QL2.P.11, combined with an offset of the entire layer.
746 The residual means are smaller in figure 5.6b indicating that QL2.P.8 is less misaligned
747 overall than QL2.P.11; however the relative local offsets range between $\pm 200 \mu\text{m}$ so they are
748 still significant considering the order on which the chambers must be sensitive to position,
749 $\sim 100 \mu\text{m}$.

750 5.7 Systematic uncertainty

751 The statistical uncertainty on the local residual means was typically around $10 - 20 \mu\text{m}$, and
752 appendix B shows that the analysis was not statistically limited by the number of triggers
753 collected for each quadruplet. The systematic uncertainties were more significant.
754 Systematic uncertainties were assigned per tracking combination as the RMS of the dis-
755 tribution of the difference in local residual means each calculated in a different way. For
756 example, the RMS associated with fitting the local residual distributions with a Gaussian or
757 double Gaussian is $25 \mu\text{m}$ for the geometrically least favourable tracking combinations. The
758 distribution is shown in appendix C.1. For geometrically similar tracking combinations (like:
759 tracks on layer 1 built from hits on layers 3 and 4, and tracks on layer 4 built from hits on
760 layers 1 and 2), the systematic uncertainty was assigned as the average RMS of both.
761 Other choices were: whether to use data collected at 2.9 kV or 3.1 kV (both are collected at
762 McGill); what cluster fitting algorithm to use; and whether or not to apply a differential non-
763 linearity (DNL) correction to the cluster y -positions. A systematic uncertainty was assigned
764 using the method above to account for the effect of each choice and quantify the robustness
765 of the mean of residuals. The reasons for each choice are listed below.
766 Data taken at 3.1 kV was used over 2.9 kV because the strip and wire tracking efficiency
767 increases with higher voltage [59] (appendix C.2).
768 The Minuit2 package [65] was used to fit clusters over Guo's method [66] because it provided
769 automatic statistical uncertainty estimates and is the standard fit algorithm of ROOT [63]
770 (appendix C.3).
771 The DNL correction was not applied because its effect on the residual means was negligible
772 (appendix C.4).
773 A summary of the systematic uncertainties assigned for each tracking combination is given
774 in table 5.1.

Tracking geometry	Residual distribution fit function (C.1)	Cosmics data collection voltage (C.2)	Cluster fit algorithm (C.3)	Apply DNL correction or not (C.4)	Total
Similar to layer 3, fixed layers 1, 2	0.01	0.04	0.02	0.01	0.05
Similar to layer 4, fixed layers 1, 2	0.03	0.01	0.03	0.01	0.10
Similar to layer 2, fixed layers 1, 3	0.01	0.02	0.01	0.000	0.03
Similar to layer 4, fixed layers 1, 3	0.01	0.04	0.01	0.01	0.04
Similar to layer 2, fixed layers 1, 4	0.01	0.04	0.01	0.01	0.04

Table 5.1: Systematic uncertainty assigned for each analysis option, detailed in appendix [C](#).

775 The uncertainty in each mean of residuals was assigned as the sum in quadrature of the sta-
776 tistical uncertainty in the mean and the appropriate systematic uncertainty for the tracking
777 combination.

778 5.8 Discussion

779 Cosmics data is being used to calculate relative alignment parameters using two other meth-
780 ods [59]. A cross-check of this analysis would be to compare their results; however the studies
781 in appendix C show that the mean cosmics residuals are robust, so the comparison was not
782 prioritized.

783 Given that the uncertainty in the residual means is lesser than or near to the order of the
784 required position resolution of the sTGCs (100 μm [5]) they are relevant input for alignment
785 studies.

786 The relative local offsets as calculated from the mean of residual distributions provide a
787 complete picture of the relative alignment between detectors planes. In fact, cosmic muon
788 testing is the only characterization technique where the entire surface of quadruplet layers
789 can be probed since muons hits are distributed almost uniformly; the CMM [7] and x-ray
790 methods [8] depend on measurements at reference points, and test beams only have a limited
791 beam spot [6]. By looking at 2D-histograms of residual means like figure 5.6 for all tracking
792 combinations, it is easy to identify quadruplets that suffer large relative misalignment since
793 many residual means differ significantly from zero. Moreover, the pattern in the relative
794 local offsets can be used to motivate a physical interpretation of misalignments. The relative
795 local offsets can be used as a reference, cross check, or input in other alignment studies.

796 Relative local offsets cannot be used to position strips in the absolute ATLAS coordinate
797 system because there was no external reference to measure positions on all layers with re-
798 spect to. The lack of external reference means that there is not enough information to unfold
799 relative local offsets into absolute local offsets (with respect to the nominal quadruplet ge-
800 ometry). As an example, assuming that the residual on layer 2 in figure 5.4 is representative
801 of the relative local offset, the residual on layer 2 could be caused by the strips on layer 2
802 being misaligned from nominal, but it could also be caused by strips on layers 1 and 4 being
803 offset from nominal while the strips on layer 2 are in their nominal positions! Any number
804 of combinations of local offsets on layers 1, 2 and 4 could produce the residual on layer 2.
805 Absolute local offsets must be calculated another way.

806 **Chapter 6**

807 **Using x-rays to measure relative strip
808 position offsets**

809 Local offset measurements were done with the x-ray method. The reader is referred to the
810 paper describing the x-ray method [8], although some minor changes have been made to the
811 experimental setup since it was written. The experimental setup described here is current
812 and was used to collect the data presented in this thesis.

813 **6.1 Experimental setup**

814 The x-ray tests were performed after the quadruplets arrived at CERN, were assembled into
815 wedges, and alignment platforms installed. Essentially, an x-ray gun was attached to one
816 of the alignment platforms glued to the surface of the wedge and the x-ray beam profile
817 recorded by the strips.

818 The wedges were installed on carts that could rotate their surface to a horizontal position. A
819 mounting platform was installed on top of the alignment platform using a three-ball mount.
820 The x-ray gun used was an [Amptek Mini-X tube](#). The gun was placed in a brass holder
821 with built-in 2 mm collimator and 280 μm copper filter. The holder was mounted on one
822 of five positions on the mounting platform, as shown in figure 6.1. Gun positions were
823 chosen to avoid wire support structures in the sTGCs that reduce hit efficiency [59] and
824 boundaries between sets of strips read out by two different ASICs that could each have
825 different thresholds.

826 As with cosmics data collection, each sTGC also needed gas and high voltage to operate.

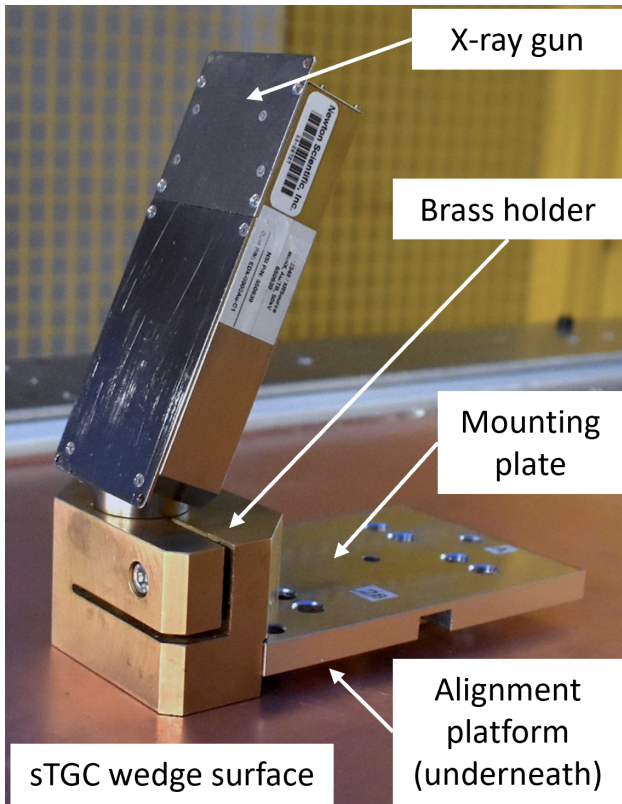


Figure 6.1: The x-ray gun mounted to the alignment platform on the surface of the wedge.
Adapted from [8].

827 Each layer was operated at 2.925 kV with high voltage from a NIM crate. The chambers
828 were flushed with CO₂ before and during data collection.

829 The gun produced x-rays with energies under 40 keV with peaks in the 7-15 keV range. The
830 x-rays mostly interacted with the wedge's copper electrodes and gold-plated tungsten wires
831 via the photo effect. The resulting photoelectrons caused ionization avalanches that were
832 picked up by the strips.

833 6.2 Data acquisition

834 A different version of the same front end electronics, but the same ASIC, as used in cosmics
835 testing were used for the x-ray testing to amplify the data and measure the peak signal
836 amplitude. Data was collected for two minutes per gun position with random triggers. A
837 trigger recorded all signals above threshold. Pad and wire data was not recorded.

838 6.3 Data preparation

839 Like with cosmics analysis, a default pedestal is subtracted from the signal peak amplitude
840 on each electrode.

841 Clusters are defined as groups of contiguous strip hits collected within 75 ns. The peak signal
842 amplitude of each electrode in a cluster is fit with a Gaussian, and the mean of the Gaussian
843 is taken as the cluster position. Cluster positions are corrected for DNL (see definition in
844 appendix C.4). Only clusters composed of hits on 3-5 strips were used in the x-ray analysis.
845 Clusters with signal on more than 5 strips were cut because they were most likely caused by
846 photoelectrons ejected with enough energy to be δ -rays.

847 The x-ray analysis diverges entirely from the cosmics analysis algorithm here because the
848 x-rays do not leave tracks. The signals picked up by the strips are from photoelectrons
849 liberated from the metals of the sTGCs, which only travel through one gas volume and are
850 ejected at all angles. Instead of creating tracks, the cluster position distribution on each
851 layer is used to define the beam profile. A typical beam profile is shown in figure 6.2.

852 6.4 Measuring local offsets

853 The mean of the cluster position distribution is taken as the x-ray beam profile center.
854 The expected center is calculated assuming a wedge with nominal geometry given the gun



Figure 6.2: Distribution of x-ray cluster mean positions after the analysis cuts and corrections. The strip cluster multiplicity, m , was limited to 3, 4 and 5. The red curve is a Gaussian fit of the distribution and the pink dashed lines denote the edges of the strips [8].

position, corrected for: the geometry of the brass holder, the positioning and angle of the alignment platforms and the beam angle. The difference between the expected and reconstructed beam profile center is a measure of the local offset. Applying the logic of equation 5.1 to the beam profile, the Gaussian mean of cluster positions on the given layer acts as the recorded position, y_i , the expected center is $y_{nom,i}$ and the local offset is $d_{local,i}$ as before, where i denotes the layer. Since the position of the alignment platforms will be monitored by the alignment system in ATLAS [5], the position of the strips that should have been at the gun position are shifted by $d_{local,i}$ and so are known in the ATLAS coordinate system for every position where x-ray data was taken.

The x-ray working group accepted an uncertainty of 120 μm on the beam profile centers. The largest uncertainty comes from the effect of the gun angle, which proved difficult to measure and correct for.

The local offsets are not presented here as the author did not conduct this work. However, the author used the local offsets to calculate relative local offsets.

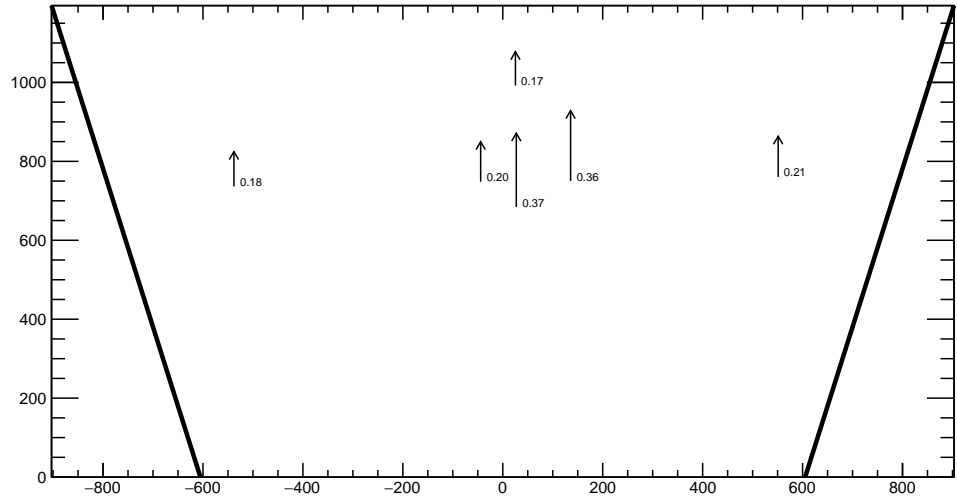
6.5 Measuring relative local offsets

The x-ray local offsets were shown to be correlated with the local offsets calculated from the CMM data, but the CMM data does not include the effect of inter-layer misalignments so the degree of correlation measurable was limited. Cosmics data is affected by inter-layer misalignments. Since the local offsets for x-rays and cosmics data are measured in different coordinate systems, they cannot be compared directly. Bringing the cosmics relative local offsets into an absolute coordinate system is impossible; however, the x-ray local offsets can be brought into a relative coordinate system.

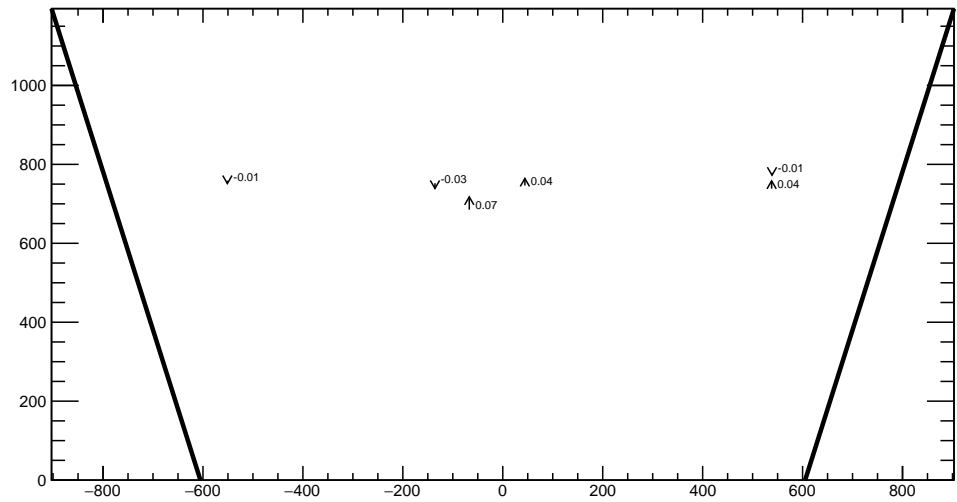
The measured x-ray beam profile centers were systematically affected by local offsets in the same way as the mean cosmics residuals, as modeled by equation 5.1. Therefore, if a 2-layer track is built from the beam profile centers on each layer and the residual calculated on a third layer, that residual should match the local mean cosmics residual. The residual is the difference between the beam profile center on the layer of interest and the polated track position from the beam profile centers recorded on the two fixed layers. The beam profile center on the layer of interest acts as y_i and the polated track position acts as $y_{track,i}$ in equation 5.2.

The built track is not an actual track of the x-ray beam. A beam profile center is actually the Gaussian mean of all selected mean cluster positions recorded during the x-ray data taking period, not a single hit of a track. Building an “abstract” track was necessary because

- 888 the x-rays cause signal in the chamber via the photoeffect so there were not individual “x-
889 ray tracks” to record. In fact the x-ray data could be collected separately for each layer.
890 Nonetheless, since the effect of local offsets on the beam profile centers was the same as their
891 effect on the recorded cosmics cluster positions the difference in algorithm between x-ray
892 and cosmics analysis was allowed.
- 893 For each x-ray survey position, the x-ray residual was calculated for all possible tracking
894 combinations (which required an x-ray beam profile on at least three layers). The x-ray
895 residuals on layer 2 calculated from the beam profile centers recorded on layers 1 and 3 are
896 represented as arrows in figure 6.3 as arrows for QL2.P.11 and QL2.P.8. For QL2.P.11, a
897 negative offset at all x-ray survey positions is clear.



(a) QL2.P.11 x-ray residuals on layer 2, reference layers 1 and 3.



(b) QL2.P.8 x-ray residuals on layer 2, reference layers 1 and 3.

Figure 6.3: The x-ray residuals on layer 2 calculated from the beam profile centers recorded on layers 1 and 3 for QL2.P.11 and QL2.P.8. The arrows originate from the expected position of the beam profile center assuming a nominal geometry, and the lengths are proportional to the calculated x-ray residuals. The tip of the arrow represents where the recorded hit was with respect to where it should have been recorded nominally. The value of the x-ray residuals are annotated in millimeters and have an uncertainty of ± 0.15 mm.

898 The uncertainty on the x-ray residuals was the error propagated through the tracking, taking
899 an uncertainty of 120 μm on each beam profile center. The uncertainty on the x-ray residuals
900 ranged from 0.15 mm to 0.4 mm from the most to least geometrically-favourable tracking
901 combination. There is no discernible pattern to the x-ray residuals on QL2.P.8 because they
902 are smaller than the uncertainty. The x-ray residual uncertainties are significantly larger
903 than the uncertainties on the relative local offsets calculated with cosmics data.

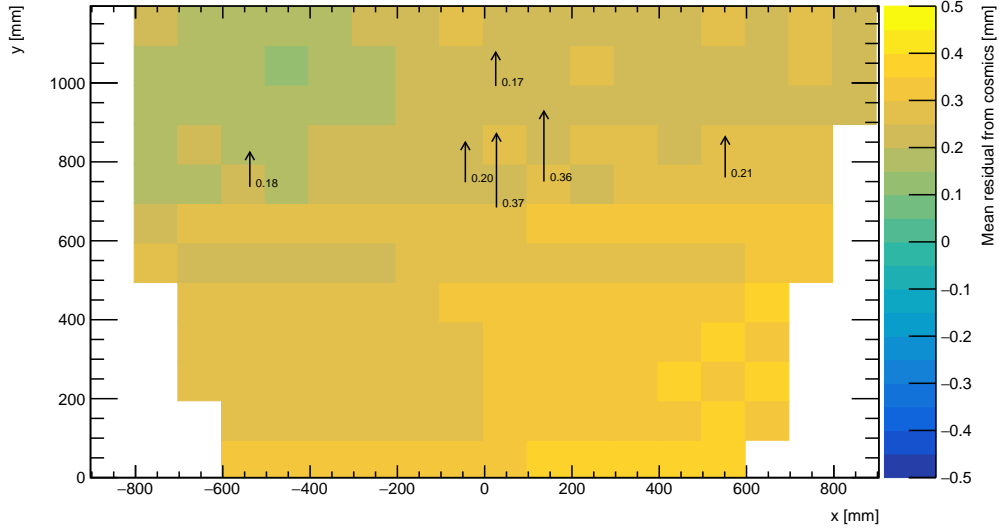
904 **Chapter 7**

905 **Comparing cosmic muon and x-ray
906 relative strip position offsets**

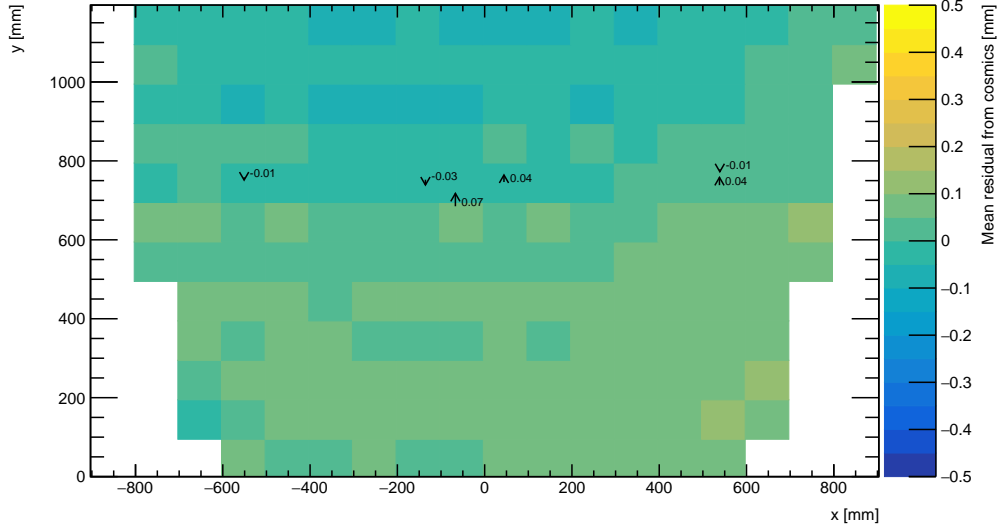
907 The goal was to validate the local offsets extracted from the x-ray data with cosmics data.
908 The complication was that the x-ray dataset provided absolute local offsets while the cosmics
909 dataset provided relative local offsets, which could not be compared directly. The solution
910 was to use the x-ray local offsets to calculate relative local offsets. The x-ray relative local
911 offset is the x-ray residual reconstructed from an abstract track using the beam profile
912 centers on each layer as the track hits. The cosmics relative local offset was taken as the
913 Gaussian mean of muon track residuals in a 100 mm by 100 mm area, referred to as the
914 mean cosmics residual. Relative local offsets of each type calculated using the same
915 reference layers are compared for each area where x-ray data is available. The results of the
916 comparison are presented here.

917 **7.1 Assessing correlation**

918 The 2D visualizations of the mean cosmics and x-ray residuals for tracks on layer 2 with
919 reference layers 1 and 3 on QL2.P.11 and QL2.P.8 are shown in figure 7.1. Figure 7.1 is a
920 superposition of figures 5.6 and 6.3.



(a) QL2.P.11 residuals of tracks on layer 2, reference layers 1 and 3.



(b) QL2.P.8 residuals of tracks on layer 2, reference layers 1 and 3.

Figure 7.1: The mean cosmics residuals are shown using colour. The x-ray residuals available at nominal gun positions are drawn as arrows and the value of the residual annotated in millimeters with uncertainty ± 0.15 mm. The length of the arrows is 500 times the value of the x-ray residual, scaled for visibility. These plots are a superposition of figures 5.6 and 6.3.

921 Figure 7.1a shows that for QL2.P.11 the x-ray residuals are of the same sign and order as
922 the mean cosmics residuals, as can be seen by comparing the the annotated value of the
923 x-ray residual to the mean cosmics residual represented by colour; QL2.P.11's mean cosmics
924 and x-ray residuals are correlated to some degree. For QL2.P.8, the x-ray residuals are of
925 the right order compared to the mean cosmics residuals, but the correlation is less apparent.
926 While x-ray residuals do not reveal a pattern across the layer's surface, the mean cosmics
927 residuals show a structure to the relative local offsets since they vary smoothly over the
928 surface of layer 2.

929 The comparison of mean cosmics and x-ray residuals was done for several quadruplets for
930 all tracking combinations (not just layer 2 residuals calculated with fixed layers 1 and 3 like
931 in figure 7.1). Scatter plots of the x-ray and mean cosmics residuals on QL2.P.11 and -2
932 for all tracking combinations shown in figures 7.2 and 7.3 reveal the degree of correlation
933 between the datasets. In the correlation plots, each rectangle is centered on the value of a
934 mean cosmics and x-ray residual pair calculated with a given tracking combination for every
935 gun position where data is available; the height and width of the squares are the uncertainty
936 in the mean cosmics and x-ray residuals respectively. Note that in the scatter plots, the
937 regions of interest where cosmics tracks are included in the calculation of mean of residuals
938 are exactly centered on the nominal x-ray beam position, unlike in figure 7.1.

939 The fitted slope and offset in figure 7.2 show that the two QL2.P.11 datasets are correlated.
940 The large uncertainty on the x-ray residuals set a limit on the sensitivity of the analysis,
941 for if the absolute value of the x-ray residuals of a quadruplet were smaller than the x-ray
942 residual uncertainties, no conclusion about the correlation could be drawn, like for QL2.P.8
943 (figure 7.3). This result is reflected in the small x-ray residuals shown in figure 7.1b that
944 do not reveal a pattern in the relative local offsets across the surface of layer 2. However,
945 figure 7.3 shows that the x-ray and mean cosmics residuals are centered around zero, as is
946 expected for a quadruplet with small relative misalignments between layers.

947 There are three patterns in the residuals on the scatter plot explained by geometry. First,
948 for both datasets the uncertainty in the extrapolated track residuals were larger than the
949 interpolated track residuals because of the extrapolation lever arm. For the x-ray residuals,
950 the effect of the lever arm on the uncertainty was direct since the residual was calculated from
951 a single abstract track; for the mean cosmics residuals it was the widening of the residual
952 distribution due to the extrapolation lever arm that increased the uncertainty in the fitted
953 mean of residuals. Second, residuals calculated through extrapolation tend to be larger
954 because the extrapolation lever arm can produce more extreme values of the track position
955 on the layer of interest. Third, the points in figure 7.2 are geometrically correlated (e.g.
956 they seem to be roughly mirrored around the origin). This is expected since the residuals
957 calculated using a given set of three layers should be geometrically correlated by the local

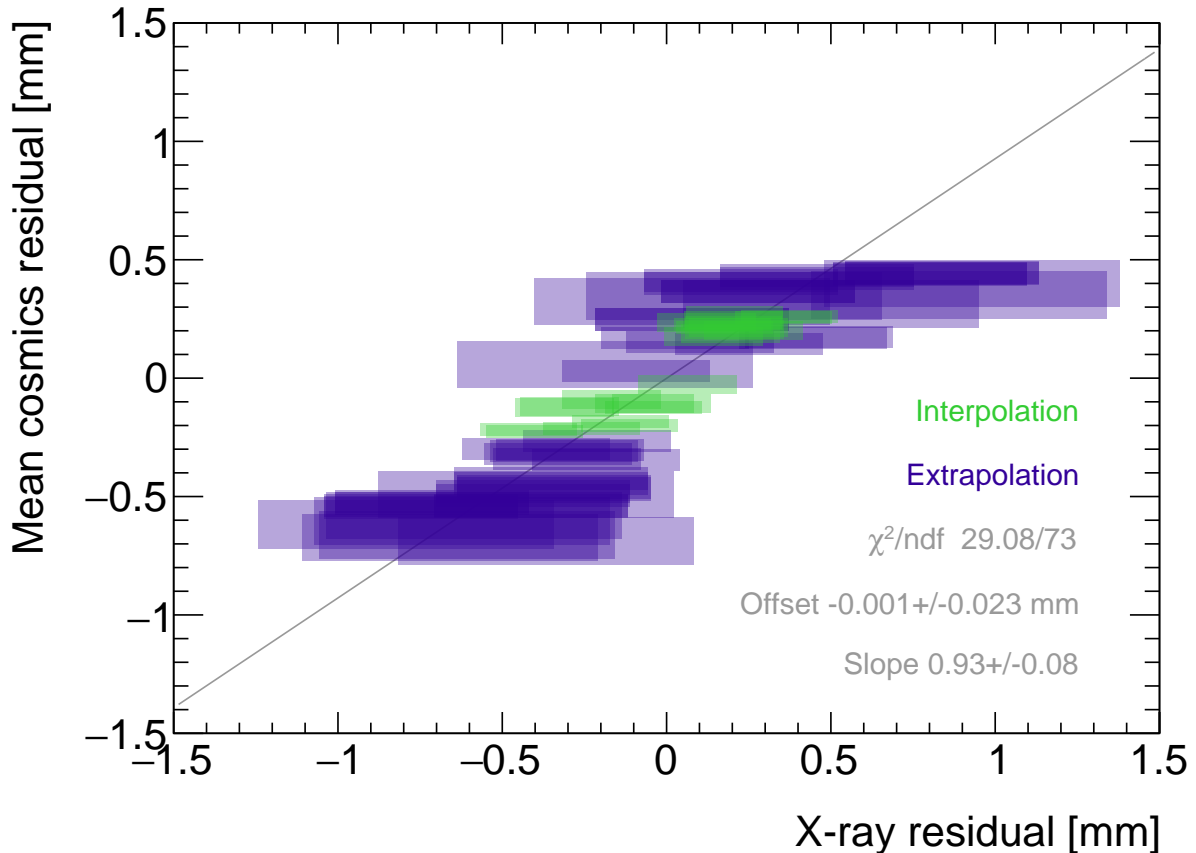


Figure 7.2: Correlation plot between x-ray and mean cosmics residuals for all tracking combinations for QL2.P.11. Each rectangle is centered on an x-ray and mean cosmics residual pair calculated at a given gun position and for a certain tracking combination. The width of the rectangles in x and y are the uncertainty in the x-ray and mean cosmics residual respectively. A printer-friendly version of this plot is available in appendix D.

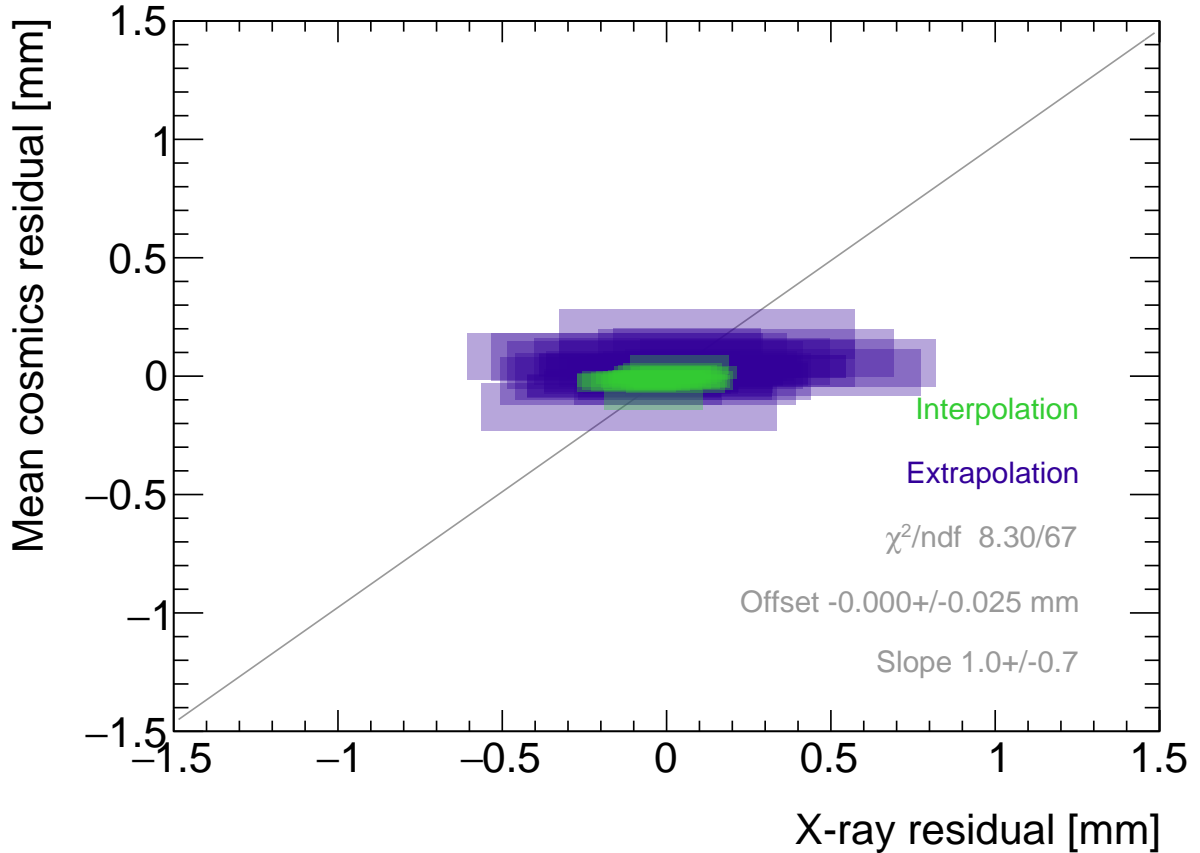


Figure 7.3: Correlation plot between x-ray and mean cosmics residuals for all tracking combinations for quadruplet 2. Each rectangle is centered on an x-ray and mean cosmics residual pair calculated at a given gun position and for a certain tracking combination. The width of the rectangles in x and y are the uncertainty in the x-ray and mean cosmics residual respectively. A printer-friendly version of this plot is available in appendix D.

958 offsets on the fixed layers and the layer of interest (the $d_{local,i}$ on each layer as defined in
959 equation 5.1).

960 7.2 Discussion

961 Several quadruplets were tested for each quadruplet construction geometry built in Canada.
962 Each quadruplet fell into one of the two categories: residuals large enough to see a correlation,
963 or residuals too small to see a correlation. Since the x-ray and mean cosmics residuals
964 were measures of the relative local offsets between the layer and the two reference layers,
965 quadruplets with the largest relative misalignments had the largest range of residuals. the
966 correlation plots were an easy visual way to identify quadruplets with large relative misalign-
967 ments.

968 The most significant limit on measuring the degree of correlation between the x-ray and
969 mean cosmics residuals was the uncertainty on the x-ray residuals, which stemmed from
970 the systematic uncertainty of 120 μm in the x-ray beam profile centers used to build the
971 abstract tracks. For example, in figure 7.3 the uncertainty in the x-ray residuals makes
972 detecting correlation impossible. The x-ray method was limited primarily by the systematic
973 uncertainties in the relative alignment of the platforms and the gun, especially the gun angle.

974 The analysis of certain quadruplets was limited by the availability of data. Sometimes,
975 less than three layers were surveyed for a given x-ray gun position so no residuals could
976 be calculated. Too few x-ray residuals prevented the analysis from detecting a significant
977 correlation, should it even be measurable. Often, the analysis of smaller quadruplets (placed
978 innermost on the wheel) suffered as a result because they had fewer alignment platforms, and
979 hence gun positions, on their surfaces. The analysis was also limited to certain quadruplets.
980 The wedges constructed the earliest (typically small wedges) were surveyed when the x-ray
981 method was still being designed and so have limited x-ray residuals calculated from beam
982 profiles of lower quality. In addition, not all cosmic muon test sites had enough front end
983 electronics to collect data on three layers simultaneously, which is the minimum required to
984 be able to calculate residuals.

985 Nonetheless, the comparison of x-ray and cosmics residuals was really to confirm the x-ray
986 method's ability to measure local offsets with an independent dataset. The x-ray local offsets
987 allow the calculation of relative local offsets that have been correlated to the cosmics relative
988 local offsets. Therefore, the analysis of quadruplets with relative local offsets large enough
989 to detect a correlation validates the x-ray method's ability to measure local offsets.

990 The potential of using relative local offsets calculated from cosmics data to study relative
991 alignment between sTGC layers stands on its own. For example, although the x-ray relative

992 local offsets of QL2.P.8 in figure 7.1b do not reveal a pattern, the variation in the cosmics
993 relative local offsets do. Identifying the pattern is possible because mean cosmics residuals
994 can be calculated across the entire area and are sensitive to smaller relative local offsets since
995 their uncertainty is significantly smaller.

996 The advantage of the x-ray dataset over the cosmics dataset is that absolute local offsets
997 are measurable thanks to the reference frame provided by the alignment platforms. This is
998 required to measure the position of strips in the ATLAS coordinate system to satisfy the
999 NSWs' precision tracking goals. The x-ray local offsets are being used to build an alignment
1000 model of strips in each quadruplet. It is compelling to imagine using the cosmics relative
1001 local offsets to improve the model considering their precision and ability to capture effects
1002 across the entire area of the quadruplet.

1003 **Chapter 8**

1004 **Outlook and summary**

1005 The cosmic muon dataset was used to independently confirm the absolute local offsets mea-
1006 sured by the x-ray method. The x-ray offsets are being used to complete the sTGC alignment
1007 scheme of the NSWs: the NSW alignment system monitors the position of alignment plat-
1008 forms on the surface of sTGC wedges, and the x-ray measurements provide the offsets of
1009 the strip pattern with respect to each alignment platform. The continuation of this anal-
1010 ysis is detailed next (section 8.1) before summarizing and considering the larger context
1011 (section 8.2).

1012 **8.1 Outlook**

1013 Next all quadruplets with suitable cosmics and x-ray data should be surveyed to flag anom-
1014alous quadruplets (as a first step). If a quadruplet’s correlation plot like figure 7.2 or 7.3
1015 reveals an unexpected correlation or has a large scatter, it would indicate an issue with ei-
1016ther the cosmics or x-ray data collection to be investigated further. The uncertainty in each
1017 set of tracking points would inform the interpretation of the anomaly. Then, the quality of
1018 the correlation should be evaluated over all quadruplets instead of individually.

1019 For now, the correlation for the individual quadruplets tested support the use of the x-ray
1020 data to build an alignment model [8]. Work on creating an alignment model is ongoing.
1021 Currently, the algorithm compares the y -position of a local group of strips at each x-ray gun
1022 position as measured by the x-ray and CMM methods in a fit to extract a global slope (m)

1023 and offset (b) per layer, i , where the χ^2 is given by equation 8.1.

$$\chi^2 = \frac{[dy_{cmm,corr} - dy_{xray}]^2}{\delta dy_{xray}^2 + \delta dy_{cmm,corr}^2}, \quad (8.1)$$

1024

$$dy_{cmm,corr} = y_{cmm} + b_i + m_i x - y_{nom} \quad (8.2)$$

1025 Here, dy refers to the corrected CMM and x-ray local offsets, and δdy refers to their re-
1026 spective uncertainties. The CMM measurements were taken before the cathode boards were
1027 assembled into quadruplets, so alignment parameters for the given layer were extracted from
1028 the χ^2 fit by stepping the corrected CMM y -position towards the x-ray y -position by adjust-
1029 ing the layer's slope and offset parameters. The plan is that the alignment parameters will
1030 be provided to the ATLAS experiment's offline software to reconstruct muon tracks from the
1031 NSWs' sTGCs. The large uncertainty on the x-ray local offsets (120 μm) and the sparseness
1032 of the measurements means that including input from other characterization datasets could
1033 reduce the uncertainty on the alignment model parameters.

1034 The uncertainty in the mean cosmics residuals was smaller than the desired position reso-
1035 lution of the sTGCs, so they provide relevant information about strip positions. Moreover,
1036 they can be calculated over the entire area of the quadruplet instead of at specific posi-
1037 tions. It would be great to use the cosmics residuals as input to calculate and reduce the
1038 uncertainty on the alignment parameters. Since mean cosmics residuals can only provide
1039 relative alignment information, one idea would be to use them to constrain the fit of the
1040 alignment parameters. In this case, the alignment parameters would need to be fitted on all
1041 layers at once, and the shifting y -positions on each layer forced to create an abstracted track
1042 residual equal to the local mean cosmics residual (within uncertainty) for each x-ray point.
1043 Or, instead of constraining the fit, it could be penalized if the resulting parameters do not
1044 result in abstracted track residuals equal to the mean cosmics residuals within uncertainty.
1045 Some work on using the three datasets at once in a fit has been started.

1046 8.2 Summary

1047 The LHC [1] will be at the energy frontier of particle physics for at least the next decade,
1048 making it a unique tool with which to study particle physics. With the HL-LHC [2], high
1049 statistics on rare particle physics processes will enable more precise measurements of param-
1050 eters of the Standard Model and increase the sensitivity to signatures of physics beyond the
1051 Standard Model [3]. To capitalize on the increased collision rate, the NSWs of the ATLAS
1052 experiment must be replaced to keep the triggering and tracking performance [5].

1053 Small-strip thin gap chambers are gas ionization chambers optimized for a high rate envi-
1054 ronment [5]. Using the pad electrodes to define a region of interest makes it possible to get
1055 track segments of ~ 1 mrad angular resolution quickly, which will be used as input to check
1056 if a collision originated from the interaction point and should be triggered on or not [5, 53].
1057 sTGCs are also able to provide better than $100 \mu\text{m}$ position resolution on each detector plane
1058 to fulfill precision offline tracking requirements [6].

1059 Ultimately, the positions of the sTGC strip electrodes need to be known in ATLAS to within
1060 $\sim 100 \mu\text{m}$ so that they can deliver the required position resolution. The ATLAS alignment
1061 system will position alignment platforms on the surface of the sTGC wedge, and an alignment
1062 model will be used to position the strips with respect to the alignment platforms [5]. Input
1063 to the alignment model comes from the datasets used to characterize the quadruplets. The
1064 x-ray method [8] is used to measure offsets of strips from their nominal position to achieve
1065 this goal. The alignment model could be built on x-ray data alone, but the sparseness of
1066 and large uncertainty on the local offsets mean that the alignment model could benefit from
1067 more input. Comparing the x-ray offsets to the CMM data [7] allows the effect of inter-layer
1068 misalignments to be isolated and increases the input to the alignment model.

1069 The cosmics dataset was used to confirm the local offsets measured with the x-ray gun. It
1070 provides relative local offsets between sTGC strip layers. The 2D visualizations of relative
1071 local offsets allow personnel to quickly identify areas of misaligned strips and make hypothe-
1072 ses of the physical origin of those misalignments. The correlation seen between the x-ray and
1073 cosmics relative local offsets in quadruplets with large relative misalignments both confirms
1074 the validity of the x-ray local offsets and again is a quick way to identify quadruplets with
1075 large misalignments. Moreover, the mean of track residuals in an area is a robust estimation
1076 of the relative local offset, as shown by the estimation of systematic uncertainties; the relative
1077 local offsets for all two-fixed layer reference frames do not change by more than $100 \mu\text{m}$ given
1078 variation in data collection conditions and analysis algorithms. The cosmics relative local
1079 offsets are therefore relevant input for alignment studies and could improve the alignment
1080 model that will position each strip.

1081 Achieving the required position resolution on each layer of the NSWs in the particle track
1082 bending plane achieves the design momentum resolution for muons ejected towards the end-
1083 caps of ATLAS. Muons are important signatures of electroweak and Higgs sector events
1084 of interest for the ATLAS Collaboration’s future physics goals [5]. Being the second of two
1085 tracking technologies on the NSWs, an effective alignment model of sTGC quadruplets layers
1086 is a necessary part of making the NSWs redundant for 10 or more years of recording collisions
1087 in the High Luminosity era of the LHC.

1088 References

- 1089 [1] L Evans and P Bryant. LHC Machine. *Journal of Instrumentation*, 3(S08001), 2008.
- 1090 [2] G Apollinari, I Bejar Alonso, O Bruning, P Fessia, M Lamont, L Rossi, and L Tavian.
1091 High-Luminosity Large Hadron Collider (HL-LHC) Technical Design Report V. 0.1.
1092 Technical report, CERN, Geneva, September 2017.
- 1093 [3] A Dainese et al. The physics potential of HL-LHC. In *Input to the European Particle
1094 Physics Strategy Update*, November 2018.
- 1095 [4] The ATLAS Collaboration. The ATLAS Experiment at the CERN Large Hadron Col-
1096 linder. *Journal of Instrumentation*, 3(08):S08003, 2008.
- 1097 [5] T Kawamoto, S Vlachos, L Pontecorvo, J Dubbert, G Mikenberg, P Iengo, C Dallapic-
1098 colà, C Amelung, L Levinson, R Richter, and D Lellouch. New Small Wheel Technical
1099 Design Report. Technical report, Jun 2013. ATLAS New Small Wheel Technical Design
1100 Report.
- 1101 [6] Angel Abusleme et al. Performance of a Full-Size Small-Strip Thin Gap Chamber Pro-
1102 totype for the ATLAS New Small Wheel Muon Upgrade. *Nuclear Instruments and
1103 Methods in Physics Research Section A: Accelerators, Spectrometers, Detectors and As-
1104 sociated Equipment*, 817:85–92, May 2016. arXiv: 1509.06329.
- 1105 [7] Evan Michael Carlson. *Results of the 2018 ATLAS sTGC test beam and internal strip
1106 alignment of sTGC detectors*. Thesis, University of Victoria, Victoria, Canada, 2019.
1107 Accepted: 2019-07-16T17:20:40Z.
- 1108 [8] B. Lefebvre. Precision survey of the readout strips of small-strip Thin Gap Chambers
1109 using X-rays for the muon spectrometer upgrade of the ATLAS experiment. *Journal of
1110 Instrumentation*, 15(07):C07013–C07013, July 2020.

- 1111 [9] David J. Griffiths. *Introduction to elementary particles*. Physics textbook. Wiley-VCH,
 1112 Weinheim, Germany, 2., rev. ed., 5. reprint edition, 2011.
- 1113 [10] Michael Edward Peskin and Daniel V. Schroeder. *An introduction to quantum field
 1114 theory*. Addison-Wesley Pub. Co, Reading, Massachusetts, 1995.
- 1115 [11] P.A. Zyla et al. Review of Particle Physics. *PTEP*, 2020(8):083C01, 2020.
- 1116 [12] Makoto Kobayashi and Toshihide Maskawa. CP-violation in the renormalizable theory
 1117 of weak interaction. *Progress of theoretical physics*, 49(2):652–657, February 1973.
- 1118 [13] M. L. Perl, G. S. Abrams, A. M. Boyarski, M. Breidenbach, D. D. Briggs, F. Bulos,
 1119 W. Chinowsky, J. T. Dakin, G. J. Feldman, C. E. Friedberg, D. Fryberger, G. Goldhaber,
 1120 G. Hanson, F. B. Heile, B. Jean-Marie, J. A. Kadyk, R. R. Larsen, A. M. Litke, D. Lüke,
 1121 B. A. Lulu, V. Lüth, D. Lyon, C. C. Morehouse, J. M. Paterson, F. M. Pierre, T. P.
 1122 Pun, P. A. Rapidis, B. Richter, B. Sadoulet, R. F. Schwitters, W. Tanenbaum, G. H.
 1123 Trilling, F. Vannucci, J. S. Whitaker, F. C. Winkelmann, and J. E. Wiss. Evidence
 1124 for Anomalous Lepton Production in $\{e\}^+ \rightarrow \{e\}^- \{e\}^+ \rightarrow \{e\}^-$ Annihilation. *Physical Review Letters*, 35(22):1489–1492, December 1975. Publisher:
 1125 American Physical Society.
- 1126 [14] F. Englert and R. Brout. Broken Symmetry and the Mass of Gauge Vector Mesons.
Physical Review Letters, 13(9):321–323, August 1964. Publisher: American Physical
 1127 Society.
- 1128 [15] P. W. Higgs. Broken symmetries, massless particles and gauge fields. *Physics Letters*,
 1129 12(2):132–133, September 1964.
- 1130 [16] David Galbraith and Carsten Burgard. UX: Standard Model of the Standard Model,
 1131 November 2013.
- 1132 [17] Carlos A. Bertulani. *Nuclear physics in a nutshell*. In a nutshell. Princeton University
 1133 Press, Princeton, N.J, 2007. OCLC: ocm85690422.
- 1134 [18] Bradley W. Carroll and Dale A. Ostlie. *An introduction to modern astrophysics*. Pearson
 1135 Addison-Wesley, San Francisco, 2nd ed edition, 2007. OCLC: ocm69020924.
- 1136 [19] Mirko Boezio and Emiliano Mocchiutti. Chemical composition of galactic cosmic rays
 1137 with space experiments. *Astroparticle Physics*, 39-40:95–108, December 2012.
- 1138 [20] B. Aharmim et al. Combined analysis of all three phases of solar neutrino data from
 1139 the sudbury neutrino observatory. *Phys. Rev. C*, 88:025501, Aug 2013.

- 1142 [21] B. Pontecorvo. Neutrino Experiments and the Problem of Conservation of Leptonic
 1143 Charge. *Zh. Eksp. Teor. Fiz.*, 53:1717–1725, 1967.
- 1144 [22] S. M. Bilenky and S. T. Petcov. Massive neutrinos and neutrino oscillations. *Reviews*
 1145 *of Modern Physics*, 59(3):671–754, July 1987.
- 1146 [23] Bing-Lin Young. A survey of dark matter and related topics in cosmology. *Frontiers of*
 1147 *Physics*, 12(2):121201, April 2017.
- 1148 [24] Carlos Muñoz. Dark matter detection in the light of recent experimental results. *International*
 1149 *Journal of Modern Physics A*, 19(19):3093–3169, July 2004.
- 1150 [25] Gerard Jungman, Marc Kamionkowski, and Kim Griest. Supersymmetric dark matter.
 1151 *Physics Reports*, 267(5):195–373, March 1996.
- 1152 [26] G. Arnison et al. Experimental observation of isolated large transverse energy elec-
 1153 trons with associated missing energy at $s=540$ GeV. *Physics Letters B*, 122(1):103–116,
 1154 February 1983.
- 1155 [27] M. Banner et al. Observation of single isolated electrons of high transverse momentum
 1156 in events with missing transverse energy at the CERN pp collider. *Physics Letters B*,
 1157 122(5):476–485, March 1983.
- 1158 [28] G. Arnison et al. Experimental observation of lepton pairs of invariant mass around 95
 1159 GeV/c² at the CERN SPS collider. *Physics Letters B*, 126(5):398–410, July 1983.
- 1160 [29] P. Bagnaia et al. Evidence for $Z \rightarrow e^+e^-$ at the CERN pp collider. *Physics Letters B*,
 1161 129(1):130–140, 1983.
- 1162 [30] CDF Collaboration. Observation of Top Quark Production in
 1163 $\overline{p}p$ Collisions with the Collider Detector at Fermilab. *Physical Review Letters*, 74(14):2626–2631, April 1995. Publisher: American
 1164 Physical Society.
- 1166 [31] D0 Collaboration. Observation of the Top Quark. *Physical Review Letters*, 74(14):2632–
 1167 2637, April 1995. Publisher: American Physical Society.
- 1168 [32] The ATLAS Collaboration. Observation of a new particle in the search for the Standard
 1169 Model Higgs boson with the ATLAS detector at the LHC. *Physics Letters B*, 716(1):1–
 1170 29, September 2012. arXiv: 1207.7214.

- 1171 [33] The CMS Collaboration. Observation of a new boson at a mass of 125 GeV with the
1172 CMS experiment at the LHC. *Physics Letters B*, 716(1):30–61, September 2012. arXiv:
1173 1207.7235.
- 1174 [34] Standard Model Summary Plots June 2021.
- 1175 [35] The ALICE Collaboration. The ALICE experiment at the CERN LHC. *JOURNAL OF*
1176 *INSTRUMENTATION*, 3, AUG 2008.
- 1177 [36] ATLAS luminosity public results run-1, March 2011.
- 1178 [37] ATLAS luminosity public results run-2, July 2015.
- 1179 [38] The European Strategy for Particle Physics. Technical Report CERN/2685, CERN,
1180 2006. Adopted by the CERN council at a special session at ministerial level in Lisbon
1181 in 2006.
- 1182 [39] HiLumi HL-LHC Project. LHC/HL-LHC plan (last update january 2021). <https://hilumilhc.web.cern.ch/content/hl-lhc-project>, last accessed on 2021-09-09.
- 1184 [40] M. Cepeda et al. Report from Working Group 2: Higgs Physics at the HL-LHC and
1185 HE-LHC. *CERN Yellow Rep. Monogr.*, 7:221–584. 364 p, Dec 2018.
- 1186 [41] ATLAS inner detector : Technical Design Report, 1. Technical Report CERN-LHCC-
1187 97-016, CERN, 1997. ISBN: 9789290831020 Publication Title: CERN Document Server.
- 1188 [42] L. Rossi, S. Haywood, A. Romanouk, and R. Nickerson. ATLAS inner detector : Tech-
1189 nical Design Report, 2. Technical Report CERN-LHCC-97-017, CERN, 1997. ISBN:
1190 9789290831037 Publication Title: CERN Document Server.
- 1191 [43] ATLAS liquid-argon calorimeter : Technical Design Report. Technical Report CERN-
1192 LHCC-96-041, CERN, 1996. ISBN: 9789290830900 Publication Title: CERN Document
1193 Server.
- 1194 [44] ATLAS tile calorimeter : Technical Design Report. Technical Report CERN-LHCC-96-
1195 042, CERN, 1996. ISBN: 9789290830917 Publication Title: CERN Document Server.
- 1196 [45] ATLAS level-1 trigger : Technical Design Report. Technical Report CERN-LHCC-98-
1197 014, CERN, 1998. ISBN: 9789290831280 Publication Title: CERN Document Server.
- 1198 [46] Technical Design Report for the Phase-II Upgrade of the ATLAS TDAQ System. Tech-
1199 nical report, CERN, Geneva, Sep 2017.

- 1200 [47] Marzio Nessi, Markus Nordberg, Peter Jenni, and Kenway Smith. ATLAS high-level
1201 trigger, data-acquisition and controls : Technical Design Report. Technical Report
1202 CERN-LHCC-2003-022, CERN, 2003. Publication Title: CERN Document Server.
- 1203 [48] A Ruiz Martínez and. The run-2 ATLAS trigger system. *Journal of Physics: Conference
1204 Series*, 762:012003, oct 2016.
- 1205 [49] ATLAS magnet system : Technical Design Report, 1. Technical Report CERN-LHCC-
1206 97-018, CERN, 1997. ISBN: 9789290831044 Publication Title: CERN Document Server.
- 1207 [50] ATLAS Collaboration. Performance of the ATLAS muon trigger in pp collisions at
1208 $\sqrt{s}=8\text{ TeV}$. *The European Physical Journal C*, 75(3):120, March 2015. arXiv:
1209 1408.3179.
- 1210 [51] ATLAS Collaboration. ATLAS Muon Spectrometer: Technical Design Report. Techni-
1211 cal Report CERN-LHCC-97-022, CERN, Geneva, 1997.
- 1212 [52] S. Aefsky, C. Amelung, J. Bensinger, C. Blocker, A. Dushkin, M. Gardner, K. Hashemi,
1213 E. Henry, B. Kaplan, P. Keselman, M. Ketchum, U. Landgraf, A. Ostapchuk, J. Roth-
1214 berg, A. Schricker, N. Skvorodnev, and H. Wellenstein. The Optical Alignment System
1215 of the ATLAS Muon Spectrometer Endcaps. *Journal of Instrumentation*, 3(11):P11005–
1216 P11005, November 2008. Publisher: IOP Publishing.
- 1217 [53] E. Perez Codina. Small-strip Thin Gap Chambers for the muon spectrometer upgrade of
1218 the ATLAS experiment. *Nuclear Instruments and Methods in Physics Research Section
1219 A: Accelerators, Spectrometers, Detectors and Associated Equipment*, 824:559–561, July
1220 2016.
- 1221 [54] John Townsend. *Electricity in gases*. Clarendon Press, Oxford, 1915.
- 1222 [55] S. Majewski, G. Charpak, A. Breskin, and G. Mikenberg. A thin multiwire chamber
1223 operating in the high multiplication mode. *Nuclear Instruments and Methods*, 217:265–
1224 271, 1983.
- 1225 [56] E. Gatti, A. Longoni, H. Okuno, and P. Semenza. Optimum geometry for strip cathodes
1226 or grids in MWPC for avalanche localization along the anode wires. *Nuclear Instruments
1227 and Methods*, 163(1):83–92, July 1979.
- 1228 [57] G. Battistoni, P. Campana, V. Chiarella, U. Denni, E. Iarocci, and G. Nicoletti. Re-
1229 sistive cathode transparency. *Nuclear Instruments and Methods in Physics Research*,
1230 202(3):459–464, November 1982.

- 1231 [58] P. K. F. Grieder. *Cosmic rays at Earth: researcher's reference manual and data book*.
 1232 Elsevier Science Ltd, Amsterdam, 1st ed edition, 2001.
- 1233 [59] Benoit Lefebvre. *Characterization studies of small-strip Thin Gap Chambers for the*
 1234 *ATLAS Upgrade*. PhD Dissertation, McGill University, Montreal, Canada, 2018.
- 1235 [60] R. Keyes, K.A. Johnson, L. Pepin, F. Léger, C. Qin, S. Webster, A. Robichaud-
 1236 Véronneau, C. Bélanger-Champagne, B. Lefebvre, S.H. Robertson, A. Warburton,
 1237 B. Vachon, and F. Corriveau. Development and characterization of a gas system and
 1238 its associated slow-control system for an ATLAS small-strip thin gap chamber testing
 1239 facility. *Journal of Instrumentation*, 12(04):P04027–P04027, April 2017.
- 1240 [61] George Iakovidis. VMM3, an ASIC for Micropattern Detectors. In *Proceedings of*
 1241 *Science*, page 5, Philadelphia, 2017.
- 1242 [62] Bohan Chen. *Calibration Studies of the Front-End Electronics for the ATLAS New*
 1243 *Small Wheel Project*. PhD thesis, McGill University, Montreal, Canada, 2019.
- 1244 [63] R. Brun and F. Rademakers. ROOT: An object oriented data analysis framework.
 1245 *Nucl. Instrum. Meth. A*, 389:81–86, 1997. See also "ROOT" [software], Release 6.18/02,
 1246 23/08/2019, (<https://zenodo.org/record/3895860#.YVJW6n0pCHs>).
- 1247 [64] Fabio Sauli. Principles of operation of multiwire proportional and drift chambers. In *Cern*
 1248 *Yellow Reports: Monographs*, page 92 p, Geneva, 1977. CERN, CERN. CERN,
 1249 Geneva, 1975 - 1976.
- 1250 [65] M. Hatlo, F. James, P. Mato, L. Moneta, M. Winkler, and A. Zsenei. Developments
 1251 of mathematical software libraries for the LHC experiments. *IEEE Trans. Nucl. Sci.*,
 1252 52:2818–2822, 2005.
- 1253 [66] Hongwei Guo. A Simple Algorithm for Fitting a Gaussian Function [DSP Tips and
 1254 Tricks]. *IEEE Signal Processing Magazine*, 28(5):134–137, September 2011.
- 1255 [67] Ichita Endo, Tatsuo Kawamoto, Yoshinari Mizuno, Takashi Ohsugi, Takashi Taniguchi,
 1256 and Tohru Takeshita. Systematic shifts of evaluated charge centroid for the cathode
 1257 read-out multiwire proportional chamber. *Nuclear Instruments and Methods in Physics*
 1258 *Research*, 188(1):51–58, September 1981.
- 1259 [68] Bernd Stelzer. The New Small Wheel Upgrade Project of the ATLAS Experiment.
 1260 *Nuclear and Particle Physics Proceedings*, 273-275:1160–1165, April 2016.

- 1261 [69] Xiao Zhao, Wenlong Li, Dengfeng Zhang, Changyu Li, Han Li, Shengquan Liu, Peng
1262 Miao, Yanyan Du, Yanyun Duan, and Chengguang Zhu. Cosmic test of sTGC detector
1263 prototype made in China for ATLAS experiment upgrade. *Nuclear Instruments and Methods in Physics Research Section A: Accelerators, Spectrometers, Detectors and Associated Equipment*, 927:257–261, May 2019.
- 1266 [70] Manfred Krammer. Upgrade Programs of the LHC Experiment, November 2017.
- 1267 [71] Benoit Lefebvre. stgc_as_built_fit.
- 1268 [72] Benoit Lefebvre. tgc_analysis.
- 1269 [73] The ATLAS Collaboration. Athena.
- 1270 [74] Lia Formenti. cosmics_xray_correlation.
- 1271 [75] Siyuan Sun. sTGC_readout_sw.
- 1272 [76] G Brianti. Large Hadron Collider in the LEP Tunnel. In *Proceedings of the ECFA-CERN Workshop*, volume 1, page 352, Lausanne and Geneva, March 1984.
- 1274 [77] Letter of Intent for the Phase-I Upgrade of the ATLAS Experiment. Technical Report
1275 CERN-LHCC-2011-012. LHCC-I-020, CERN, Geneva, November 2011.
- 1276 [78] ATLAS: letter of intent for a general-purpose pp experiment at the large hadron collider
1277 at CERN. Technical Report CERN-LHCC-92-004, CERN, Geneva, 1992.
- 1278 [79] The ATLAS Collaboration. Technical Design Report for the Phase-I Upgrade of the
1279 ATLAS TDAQ System. Technical report, Sep 2013. Final version presented to December
1280 2013 LHCC.
- 1281 [80] Howard Georgi and S. L. Glashow. Unity of all elementary-particle forces. *Phys. Rev. Lett.*, 32:438–441, Feb 1974.
- 1283 [81] Luca Lista. *Statistical Methods for Data Analysis in Particle Physics*, volume 941 of
1284 *Lecture Notes in Physics*. Springer International Publishing, Cham, 2017.
- 1285 [82] K. Kodama et al. Detection and analysis of tau neutrino interactions in DONUT
1286 emulsion target. *Nucl. Instrum. Meth. A*, 493:45–66, 2002.

¹²⁸⁷ APPENDICES

1288 **Appendix A**

1289 **Uncertainty in cluster positions**

1290 **A.1 Cluster definition**

1291 A cluster is a series of contiguous strip channels on a layer with non-zero amplitude, all
1292 part of the same trigger and having the same event number [59]. Clusters result from the
1293 drift of ionization products generate in the ionization avalanche caused by a muon [54]. The
1294 peak-detector-output (PDO) of the signal on each strip of a cluster is fit with a Gaussian.
1295 The y-position of a particle as it passed through the layer is mean of the cluster, referred to
1296 here as the hit position.

1297 **A.2 Effect of fit algorithm on cluster mean**

1298 The clusters were fit with Guo's method [66] and Minuit2 for ROOT [65]. The difference in
1299 cluster means between the two algorithms is shown in figure A.1.

1300 The RMS of the distribution in figure A.1 is 57 μm , which is much larger than the statistical
1301 uncertainty in the mean for the Minuit2 algorithm, which peaks around 7 μm . An RMS of
1302 60 μm is common for data taken with most quadruplets at 3.1 kV. Therefore, the uncertainty
1303 in the y-hit positions is assigned 60 μm .

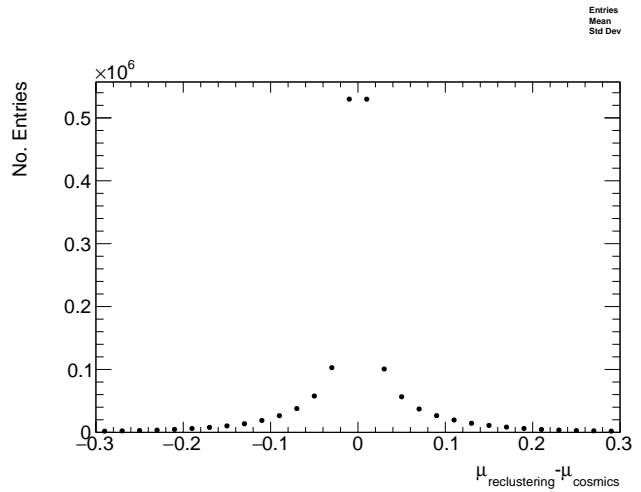


Figure A.1: The difference between cluster means calculated with Guo's method [66] in `tgc_analysis/CosmicsAnalysis` and `Minuit2` for `ROOT` [65] in `strip_position_analysis/ReClustering` for data collected with QL2.P.8 at 3.1 kV.

1304 **A.3 Effect of uncertainty in cluster mean on track residuals**

1305

1306 The uncertainty assigned to the hit position affected the uncertainty in the extrapolated/interpolated
1307 position of the track, and in the residuals. The bin size of the residual distributions was set
1308 to 200 μm because that was the uncertainty in the residuals calculated from the tracks with
1309 the least favourable geometry (like tracks built from hits on layers 1 and 2 and extrapolated
1310 to layer 4).

₁₃₁₁ **Appendix B**

₁₃₁₂ **Study of cosmics for alignment
analysis statistical uncertainty**

₁₃₁₄ Typically, one million triggers (cosmic muon events, noise, photons and δ -rays) were collected
₁₃₁₅ for each Canadian quadruplet at McGill University, resulting in roughly half the number of
₁₃₁₆ viable tracks after cuts. For QS3.P.18, 3.5 million triggers were collected. To gauge the
₁₃₁₇ sensitivity of the analysis to the available statistics, partitions of this data with each with
₁₃₁₈ a different number of triggers were analyzed separately. Ultimately, the quantity of interest
₁₃₁₉ was the gaussian mean of the residual distribution in regions of interest, so the peak in the
₁₃₂₀ distribution of the statistical uncertainty in the residual means for each area of interest for
₁₃₂₁ a specific tracking combination was used to gauge the quality of the analysis. How the peak
₁₃₂₂ in the residual mean uncertainty distribution changes with the number of triggers is shown
₁₃₂₃ in figure for tracks on layer 1 built from layers 3 and 4 [B.1](#).

₁₃₂₄ The uncertainty is already around 20 μm at 1 million triggers, suitable for distinguishing
₁₃₂₅ differences in offsets of order 50 μm as required. Although increased statistics could decrease
₁₃₂₆ the statistical uncertainty, it is not required for the goals of this analysis. Moreoever, the
₁₃₂₇ systematic uncertainty is around 50 μm and the systematic uncertainty on the x-ray residuals
₁₃₂₈ is 150 μm so the statistical uncertainty of 20 μm is nearly negligible.

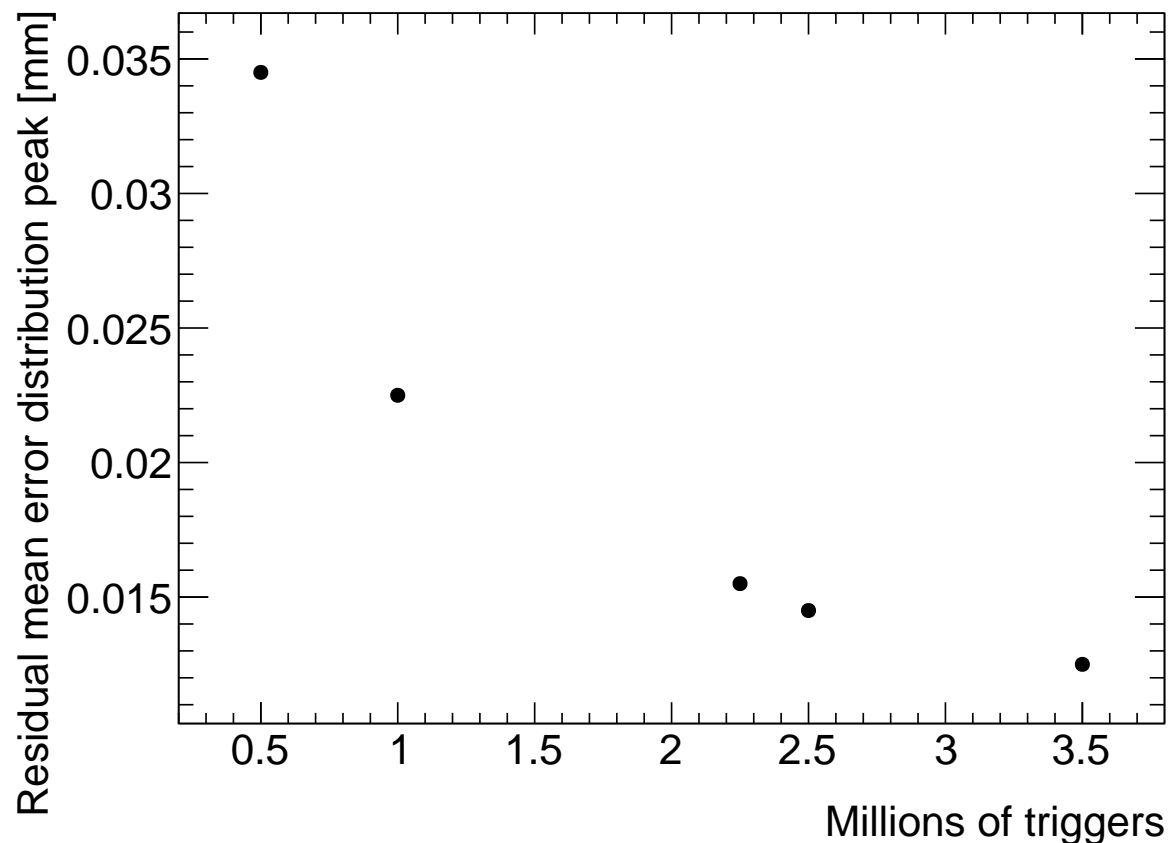


Figure B.1: How the peak of the distributions of uncertainties in the residual means in regions of interest for tracks on layer 1 built from layers 3 and 4 changed with the number of triggers used in the analysis. The distribution falls off as $\frac{1}{\sqrt{N}}$ as expected.

₁₃₂₉ **Appendix C**

₁₃₃₀ **Study of systematic uncertainties
when using cosmics data for
alignment studies**

₁₃₃₃ **C.1 Residual distribution fit function**

₁₃₃₄ The distribution of residuals should be modelled by a double gaussian fit[59]:

$$G(r) = A_s \exp\left[\frac{-(r - \mu)^2}{2\sigma_s^2}\right] + A_b \exp\left[\frac{-(r - \mu)^2}{2\sigma_b^2}\right] \quad (\text{C.1})$$

₁₃₃₅ where r is the residual, A is the gaussian amplitude, μ is the gaussian mean, σ is the
₁₃₃₆ gaussian sigma, and the subscripts s and b stand for signal and background respectively.
₁₃₃₇ One gaussian captures the real (signal) tracks and the other captures the tracks built from
₁₃₃₈ noise (background). The gaussian with the smaller width is identified as the signal.

₁₃₃₉ A single gaussian fit failed less often than a double gaussian fit. The gaussian fits were
₁₃₄₀ performed by initially estimating the amplitude to be 100 tracks, the gaussian mean to be
₁₃₄₁ the histogram mean, and gaussian σ to be the RMS. The fit range was restricted to ± 1 RMS
₁₃₄₂ from the histogram mean. The modification helped the gaussian fit capture the signal peak.
₁₃₄₃ An example residual distribution is shown in figure C.1.

₁₃₄₄ For all residual distributions in 100 mm by 100 mm bins on layer 4 built from hits on layers 1
₁₃₄₅ and 2, the difference in gaussian and double gaussian means and σ 's is shown in figure C.2.
₁₃₄₆ Since the RMS of the residual mean differences distribution is less than 50 μm the gaussian

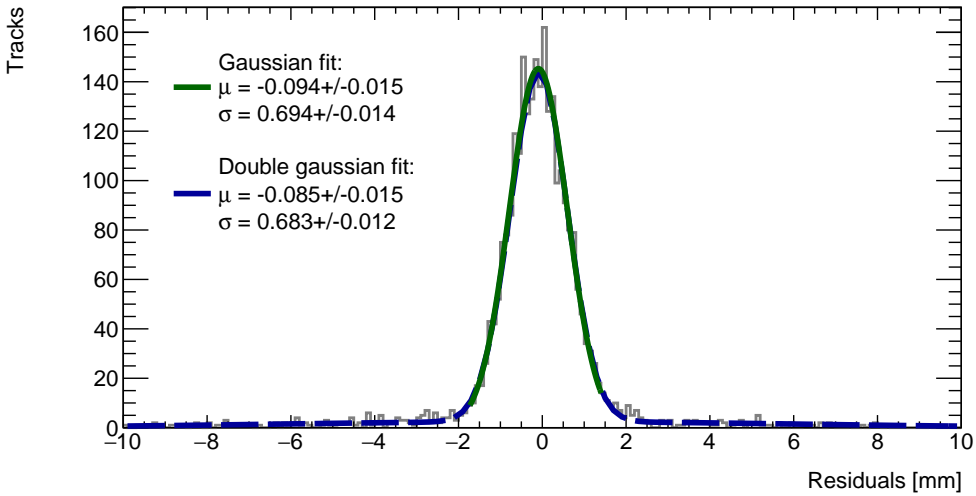


Figure C.1: Residual distribution for tracks on layer 4 built from hits on layers 1 and 2 for $x \in [-3.00, 97.00]$, $y \in [394.60, 494.60]$ mm for QL2.P.8 fit with a double gaussian and a single gaussian in a range of ± 1 RMS from the histogram mean.

1347 fit gave the same result within the required precision. Moreover, this is for the tracking
1348 combination with the worst extrapolation lever arm and the widest distribution of mean
1349 differences; the interpolation combinations have narrower distributions.

1350 The gaussian σ should be larger than the double gaussian σ because the gaussian distribution
1351 includes the effect of the noise tracks with large residuals, while the double gaussian models
1352 signal and background residuals separately. For this analysis, only the residual mean was
1353 important, so the systematic overestimate of the signal σ in the gaussian fit shown on the
1354 right of figure C.2 was allowed.

1355 C.2 Cosmic muon data collection voltage

1356 Cosmic muon data was collected at 2.9 kV and 3.1 kV because although 2.9 kV is closer to
1357 the operating conditions the chambers will be subject to in ATLAS, the extra gain provided
1358 by operating at 3.1 kV increased the signal to noise ratio for pad signals. Also, the tracking
1359 efficiency was higher with data collected at 3.1 kV. The difference in gain affected the relative
1360 population of clusters of different sizes, which in turn affected the uncertainty in the strip hit
1361 positions on each layer, the uncertainty in the track positions and the residual distributions.
1362 The residual distributions for 3.1 kV data are narrower, as shown in figure C.3.

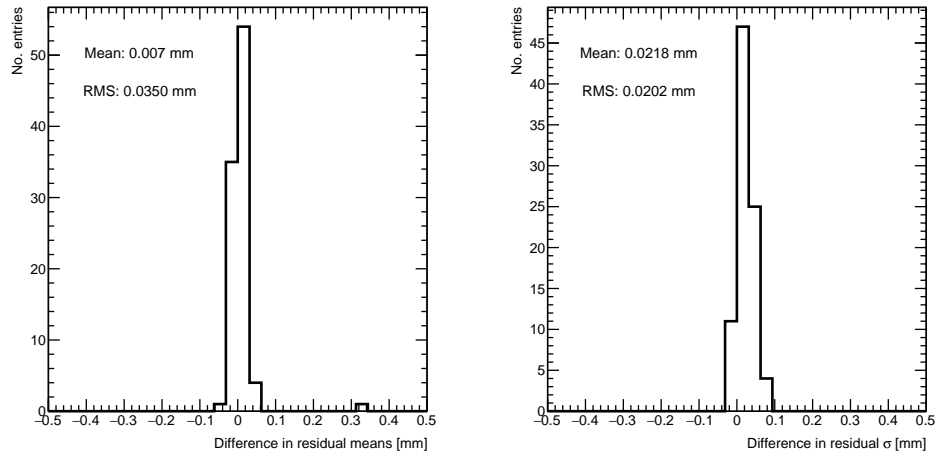


Figure C.2: Difference in residual distribution means and σ 's for a gaussian and double gaussian fit, for all residual distributions in 100 mm by 100 mm bins on layer 4 built from hits on layers 1 and 2 for QL2.P.8.

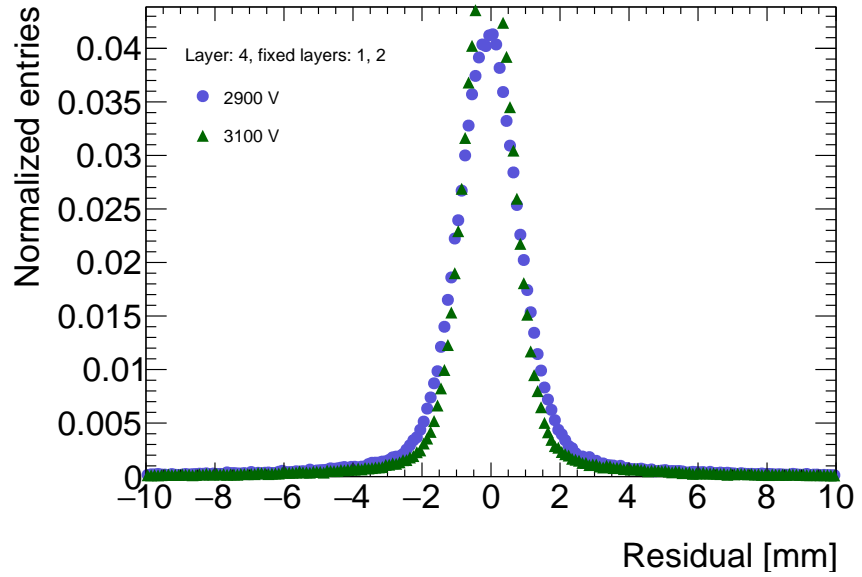


Figure C.3: Residual distribution for tracks on layer 4 built from hits on layers 1 and 2 for QL2.P.8 for data collected at 2.9 kV and 3.1 kV.

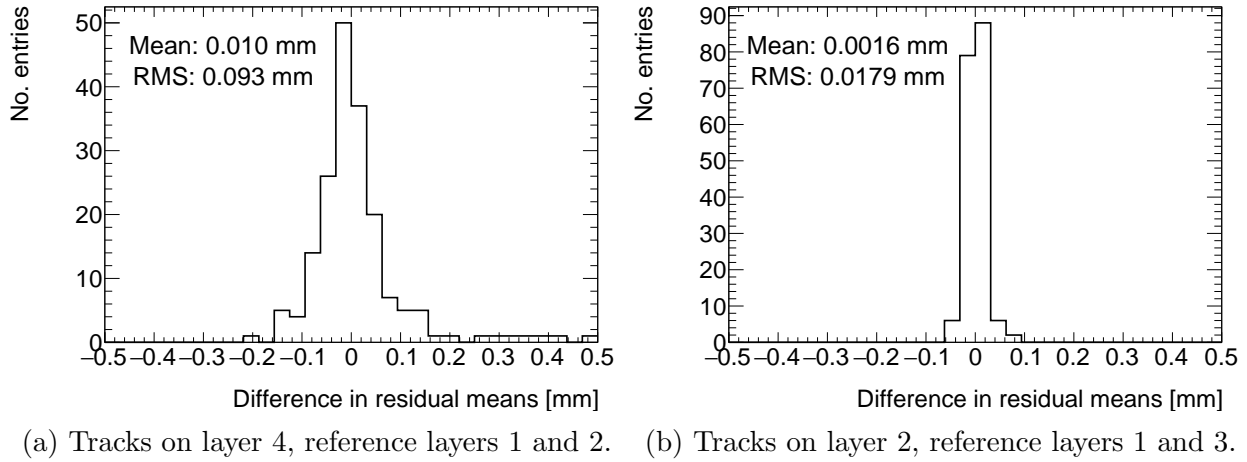


Figure C.4: Difference in residual means for data collected with QL2.P.8 at 2.9 kV and 3.1 kV respectively in 100 mm by 100 mm bins for (a) tracks on layer 4 built from hits on layers 1 and 2 and (b) tracks on layer 2 built from hits on layers 1 and 3.

1363 Neither dataset is better for calculating the mean of residuals in a given area, so a systematic
 1364 uncertainty can be assigned based on the difference in residual means calculated for 2.9 kV
 1365 and 3.1 kV data; namely, the systematic uncertainty was approximated as the RMS of the
 1366 residual mean difference distribution. Data taken with QL2.P.8 was used to estimate the
 1367 RMS, as in figure C.4a.

1368 Tracks built from hits on layers 1 and 2 and extrapolated to layer 4 have the worst lever arm
 1369 and hence the most uncertainty. The width of the distribution for geometrically favourable
 1370 tracks are much narrower. The narrowest width of the residual mean difference distribution
 1371 is for tracks on layer 2 built from hits on layers 1 and 3 (see figure C.4b).

1372 Therefore, for each tracking combination, a systematic uncertainty equal to the RMS of the
 1373 residual mean difference distribution was assigned.

1374 C.3 Cluster fit algorithm

1375 To ensure that changing the cluster fitting algorithm like in appendix A would not change
 1376 the calculated mean of residuals in each region of interest significantly, the residual means
 1377 were compared in both cases. The distribution of the difference in residual means is plotted
 1378 in figure C.5 for the tracking combination with the worst extrapolation lever arm.

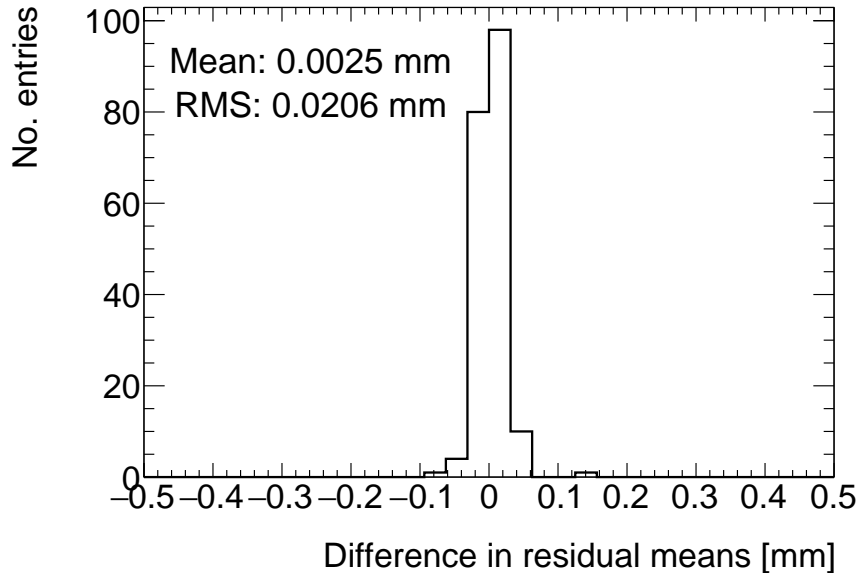


Figure C.5: Difference in residual means when the cluster fit algorithm is `Minuit2` [65] versus Guo’s method [66] for tracks on layer 4 built from hits on layers 1 and 2 for QL2.P.8.

1379 The other tracking combinations had smaller RMS values. Differences on the order of 50 μm
 1380 are important, so figure C.5 shows that the clustering algorithm had a small but notable
 1381 effect. Therefore, the RMS for each tracking combination will be used to add a systematic
 1382 uncertainty on the residual means.

1383 C.4 Differential non-linearity

1384 Definition

1385 In this context, differential non-linearity (DNL) is when the reconstructed cluster mean is
 1386 biased by the fit of the discretely sampled PDO distribution over the strips. The bias depends
 1387 on the relative position of the avalanche with respect to the center of the closest strip. For a
 1388 summary of DNL, refer to page 40 of Lefebvre’s thesis [59] and for an example application,
 1389 refer to [6].

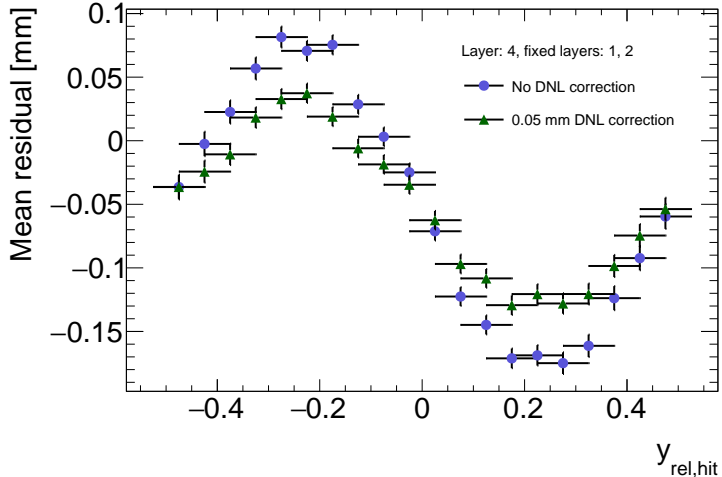


Figure C.6: Effect applying a 50 μm DNL correction to the cluster means on the residual vs y_{rel} distribution for tracks built from layers 1 and 2 and extrapolated to layer 4 for QL2.P.8.

1390 **Application and effect of DNL**

1391 The cluster mean was corrected for DNL using the equation:

$$y' = y + a \sin(2\pi y_{rel}) \quad (\text{C.2})$$

1392 where y is the cluster mean, y_{rel} is the relative position of the cluster mean with respect to
1393 the strip's center, a is the amplitude of the correction, and y' is the corrected cluster mean.
1394 The amplitude can be derived by comparing the reconstructed hit position to the expected
1395 hit position, as done in Abusleme, 2016 [6]. With cosmic muons, there is no reference hit
1396 position to compare to, so track residuals were used as a proxy [59]. The hallmark of the DNL
1397 effect is the periodic pattern in the residual versus y_{rel} profile, and the effect of correcting
1398 the cluster means using an amplitude of 50 μm is shown in figure C.6. An amplitude of
1399 50 μm was based on Lefebvre's estimate of the DNL amplitudes by layer, quadruplet and
1400 cluster size using exclusive cosmic muon tracks in `tgc_analysis/CosmicsAnalysis`. Little
1401 variation was seen in the amplitude parameters with respect to the quadruplet tested, the
1402 layer and the cluster size so a universal correction was used.

1403 Although the correction is not large enough in this case, the figure shows that the correction
1404 does reduce the DNL effect. Slightly better performance is seen in the interpolation tracking
1405 combinations where the quality of the residuals is better. DNL corrections for cosmic muon
1406 data are difficult because the DNL effect is obscured by the effect of misalignments and

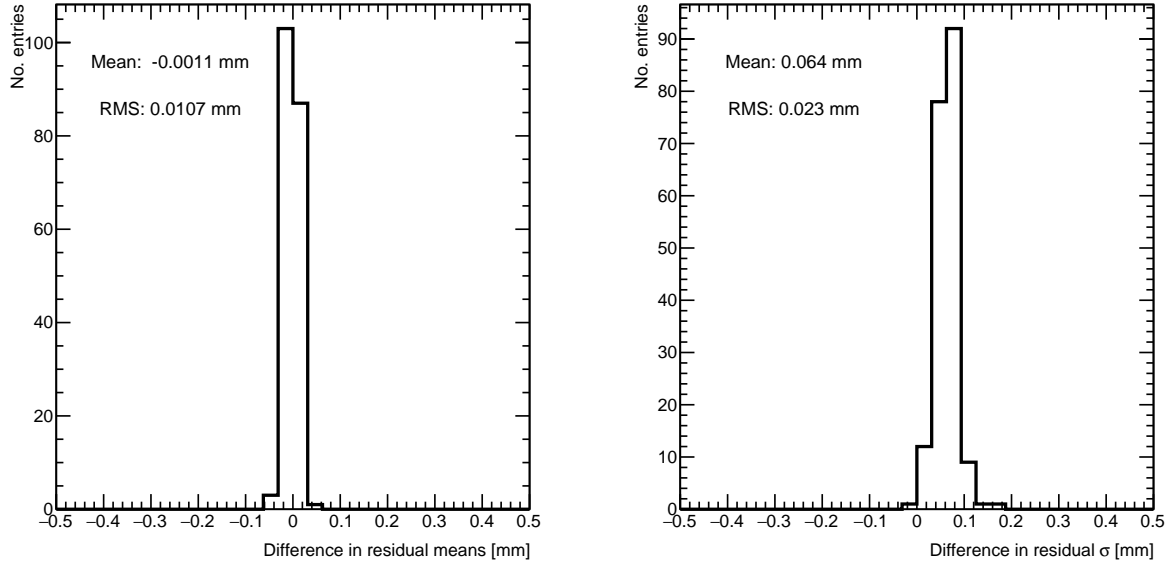


Figure C.7: Difference in residual distribution means and σ 's with and without DNL correction for residuals on layer 4 from reference layers 1 and 2 for QL2.P.8.

1407 noise. Misalignments cause the center of the sine pattern in figure C.6 to be shifted off of
1408 zero, since the mean of residuals is shifted.

1409 In figure C.7, it is apparent that the effect of the DNL correction on the mean of the
1410 residual distribution in 100 mm by 100 mm areas is on the order of micrometers in the worst
1411 extrapolation case. Although the σ 's of the residual distributions shrink with the DNL
1412 correction, the mean is the parameter of interest. Therefore, for this analysis DNL was not
1413 corrected for.

1414 The σ 's of the residual distributions do shrink with the DNL correction but not so much to
1415 affect the residual means, which are the important parameter for this analysis. Therefore,
1416 since the effect of the DNL correction is negligible, it was not pursued further.

₁₄₁₇ Appendix D

₁₄₁₈ Printable plots

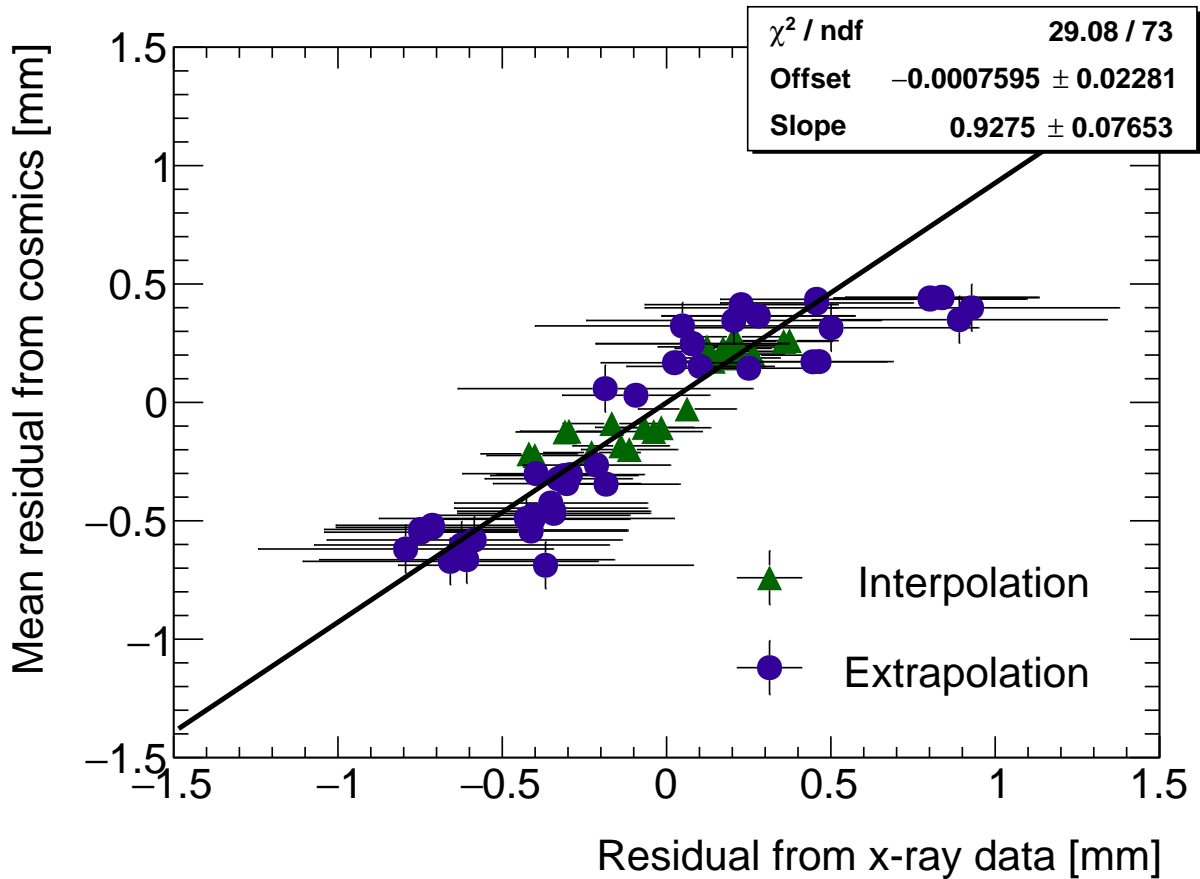


Figure D.1: Correlation plot between x-ray and cosmics residuals for all tracking combinations for QL2.P.11. Each rectangle is centered on an x-ray and mean cosmics residual pair. The width of the rectangles in x and y are the uncertainty in the x-ray and mean cosmics residual respectively. This is a printable version of figure 7.2 in section 7.1.

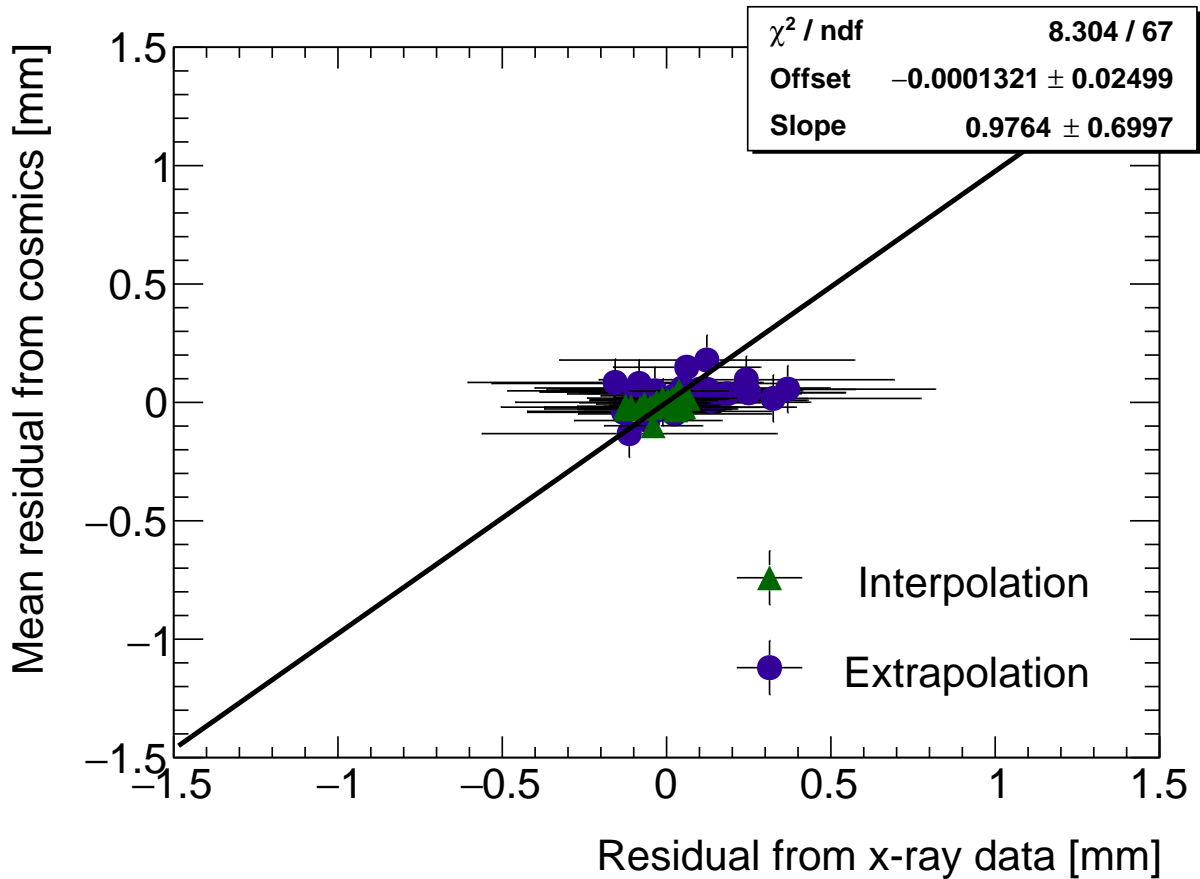


Figure D.2: Correlation plot between x-ray and cosmics residuals for all tracking combinations for QL2.P.8. Each rectangle is centered on an x-ray and mean cosmics residual pair. The width of the rectangles in x and y are the uncertainty in the x-ray and mean cosmics residual respectively. This is a printable version of figure 7.3 in section 7.1.